Preprint of: Garcia-Aristizabal et al. (2015), *Natural Hazards, 75:289-320*
doi: 10.1007/s11069-014-1324-z

Analysis of non-stationary climate-related extreme events considering climate change scenarios: an application for multi-hazard assessment in the Dar es Salaam region, Tanzania

Alexander Garcia-Aristizabal · Edoardo Bucchignani, · Elisa Palazzi, · Donatella D'Onofrio, · Paolo Gasparini, · and Warner Marzocchi

Reference: Garcia-Aristizabal A, E. Bucchignani, E. Palazzi, D. D'Onofrio, P. Gasparini, and W. Marzocchi (2015), Analysis of non-stationary climate-related extreme events considering climate change scenarios: an application for multi-hazard assessment in the Dar es Salaam region, Tanzania, *Natural Hazards*, 75:289-320, doi: 10.1007/s11069-014-1324-z

Abstract In this paper we have put forward a Bayesian framework for the analysis and testing of possible non stationarities in extreme events. We use the Extreme Value theory to model temperature and precipitation data in the Dar es Salaam region, Tanzania. Temporal trends are modeled writing the location parameter of the Generalized Extreme Value distribution in terms of deterministic functions of explanatory covariates. The analyses are performed using synthetic time series derived from a Regional Climate Model. The simulations, performed in an area around the Dar es Salaam city, Tanzania, take into account two Representative Concentration Pathways scenarios from the Intergovernmental Panel on Climate Change. Our main interest is to analyse extremes with high spatial and temporal resolution and to pursue this requirement we have adopted an individual grid box analysis approach. The approach presented in this paper is composed of the following key elements: (1) an advanced Bayesian method for the estimation of model parameters, (2) a rigorous procedure for model selection, and (3) uncertainty assessment and propagation. The results of our analyses are intended to be used for quantitative hazard and risk assessment and are presented in terms of hazard curves and probabilistic hazard maps. In the case study we found that for both the temperature and precipitation data, a linear trend in the location parameter was the only model performing better than the stationary one in the areas where evidence against the stationary model exists.

Keywords non-stationary extreme events · climate change · multi-hazard · Bayesian inference · Extreme precipitation · Extreme temperature · Dar es Salaam, Tanzania

This research has been funded by the FP7 European project CLUVA (Climate change and Urban Vulnerability in Africa).

A. Garcia-Aristizabal · P. Gasparini
Center for the Analysis and Monitoring of Environmental Risk (AMRA), Via Nuova Agnano 11, 80123 Naples, Italy
Tel.: +39-081-7685125
Fax: +39-081-7685144
E-mail: alexander.garcia@amracenter.com

Edoardo Bucchignani
Centro Euro-Mediterraneao sui Cambiamenti Climatici (CMCC)-CIRA, Capua, Italy

E. Palazzi
Institute of Atmospheric Sciences and Climate (ISAC)-CNR, Turin, Italy

D. D'Onofrio
Department of Physics, Università di Torino, Turin, Italy

W. Marzocchi
Istituto Nazionale di Geofisica e Vulcanologia, Rome, Italy

1 Introduction

Extreme meteorological phenomena such as heavy precipitation, extreme temperature (and heat waves), or strong winds, may have considerable impacts on the economy, infrastructure, health, as well as may represent a non negligible threat for human life (e.g., Stephenson et al 2008). A changing climate may lead to changes in the frequency, intensity, spatial extent, duration, and timing of weather and climate extremes, and can result in unprecedented extreme events (IPCC 2012). This study is aimed at investigating meteorological extreme events and the possible existence of trends in the extremes under climate change conditions. The Extreme Value Theory (EVT) is an approach used for the estimation of extreme values, and the distinguishing fea-

ture of an extreme value (EV) analysis is the quantification of the stochastic behavior of a process at unusually large (or small) levels. Therefore, it aims at deriving a probability distribution of events at the far end of the upper or lower ranges of the probability distributions (e.g., Coles 2001). EVT is used then to determine the probability of occurrence of events that are mainly outside of the observed data range; for this reason the EVT has found a wide spectrum of applicability in different fields, and among them, in the analysis of climatological data (e.g., Jenkinson 1955; Coles 2001; IPCC 2012).

General Circulation Models (GCM) are generally used to simulate the earth system components and their interactions, and to provide future climate projections under different emission scenarios. However, due to the coarse spatial resolution, their output generally cannot be used for impact studies on local scales, which makes it necessary the generation of higher resolution climate data (e.g., Carter et al 2007; IPCC 2012). Non-hydrostatic Regional Climate Models (RCMs) represent the atmospheric dynamics and convective precipitation processes at higher resolution compared to their hydrostatic counterpart and to the GCMs, thus providing a better description of the phenomena forced by orography or by coastal lines and a more detailed information on climate extremes (e.g., IPCC 2012). A further increase of the resolution of the climatic information coming from RCMs can be achieved by means of statistical or stochastic downscaling techniques, which do not require excessive computational efforts and allow for an estimation of the uncertainty associated to the small-scale fields (von Hardenberg et al 2007; Brussolo et al 2008).

In this work, we use the EVT to model extreme precipitation and temperature events in the Dar es Salaam region, Tanzania (Fig. 1). From the general domain used for the regional simulations (Fig. 1a), we have considered an area of about 240×240 km^2 (30×30 nodes of the domain, as seen in Fig. 1b) that covers a wide area over the Dar es Salaam region and parts of the Pwani and Morogoro regions. The data used are synthetic time series derived from the output of climate simulations performed using a RCM and taking into account two emission scenarios from the Intergovernmental Panel on Climate Change (IPCC). The EV analysis has been also applied to the RCM precipitation data further downscaled using a stochastic rainfall downscaling procedure.

The basis for the EV analysis is the Generalized extreme-value (GEV) distribution (Jenkinson 1955). To estimate the GEV model parameters in presence of non-stationary conditions we have implemented a Bayesian method that provides a natural framework to incorporate all the available sources of information and to handle uncertainties. We discuss in particular the issue of selecting the prior distributions in the parameter space, one of the main problems to be solved in Bayesian data analysis. To account for possible non-stationary conditions, we have implemented a practical covariate approach (Coles 2001) that is increasingly being used in non-stationary EV problems (e.g., Coles 2001; Katz et al 2002; Zhang et al 2004; El Adlouni et al 2007; Cannon 2010; Katz 2010; Ouarda and El-Adlouni 2011; Seidou et al 2011, 2012).

Our analyses are oriented towards producing results with high spatial and temporal resolution in order to be used as the hazard input in quantitative risk assessments. Therefore, the outputs are represented in terms of hazard curves and high resolution probabilistic maps showing the spatial distribution of the intensity values of the analyzed variables for given exceedance probability thresholds. The resulting procedure provides a unified framework that allows harmonizing the results of a variety of climate-related data and hazards, which is one of the fundamental requirements for multi-hazard and multi-risk analyses (Marzocchi et al 2012).

2 Analysis Methods

EV analysis is generally performed using either the Block maxima approach (adopted in this study, in which the GEV family is applied to the largest intensity measure z in a selected period of time), or the peaks-over-threshold approach (in which the Generalized Pareto distribution is applied to peaks of independent z values exceeding a sufficiently high threshold). Most studies perform analyses of extreme events under the assumption of stationarity. However, the current evidence that the hydroclimatic system may be non-stationary on the time scales relevant for EV analyses (e.g., among others, Zwiers and Kharin 1998; Houghton et al 2001; Jain and Lall 2001; Solomon et al 2007) makes of the stationarity a questionable hypothesis. Therefore, it is necessary to apply methods that explicitly allow for testing non-stationarity in the distribution parameters (Coles 2001). This requirement becomes more evident when analyzing climatological data derived from climate simulations in which emission scenarios have been considered.

The intensity of climate-related hazards shows variations in space and this motivates the increasing interest for the spatial modeling of extremes. Examples of statistical approaches that have been proposed include Bayesian hierarchical models, copulas, and max-stable random fields (e.g. Davison et al 2012). These approaches become fundamental for modeling spatial

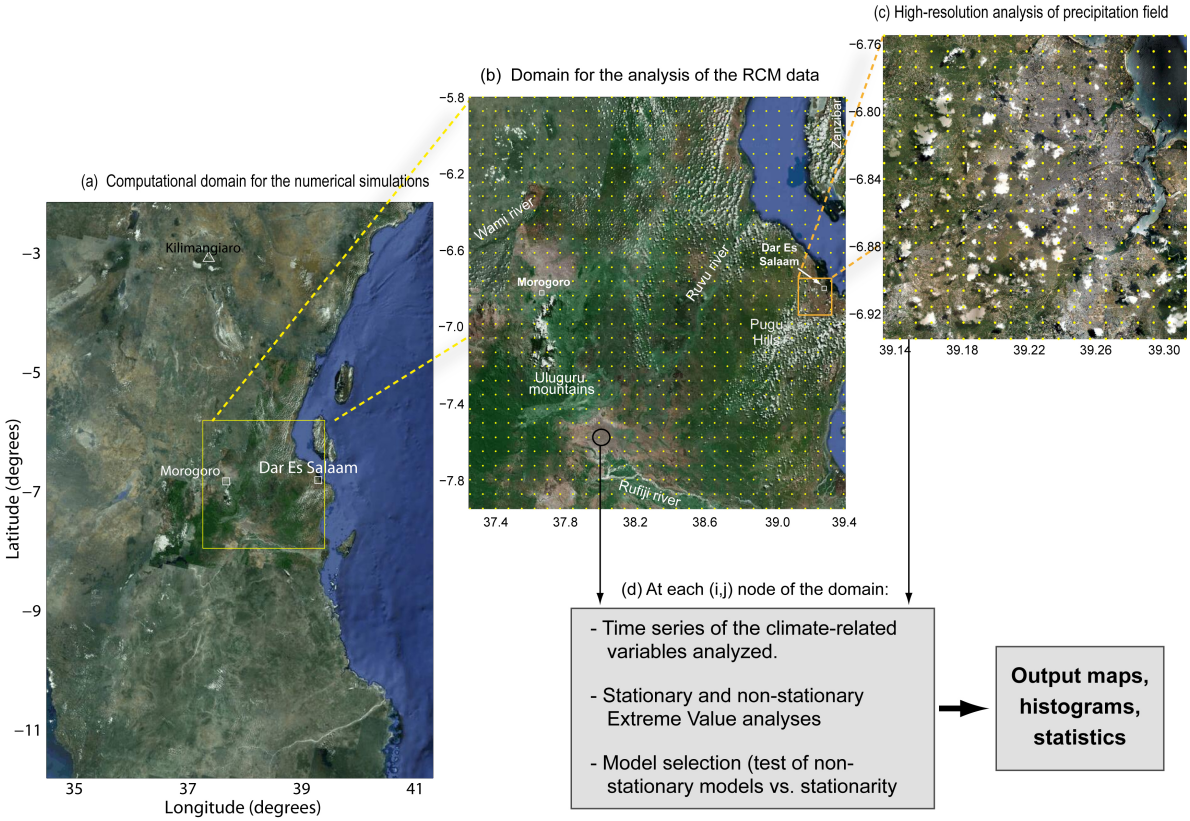

Fig. 1 Maps showing the study area around Dar es Salaam, Tanzania. (a) Computational domain used for the numerical simulations with the regional model COSMO-CLM; the rectangle shows the part of the domain used for the analysis of extreme events. (b) Area of the domain used for the analysis of extreme events; the 8×8 km resolution calculation grid is also shown. (c) Domain used for the stochastic downscaling of the precipitation data (1×1 km resolution). (d) Summary of the process adopted for the analysis of extremes (for details, see the text).

processes defined on the continuum but observed only at fixed sites x of a spatial domain $\mathcal{X}$, and for which interpolation may be necessary. The statistical problem in this case is to make inference for the process in the whole domain (e.g. Sang and Gelfand 2010; Atyeo and Walshaw 2012; Davison et al 2012).

In our work we use "areal data" generated by a high-resolution RCM; the data, therefore, is available at a set of evenly-distributed points corresponding to the model grid. Note that the physical modeling of the process intrinsically provides the consistency and spatial correlation to the data. As a preliminary step in the analysis, we investigate the spatial coherence of the various model variables, by calculating, for each of them, the correlation between the time series at a model grid point (node) and the time series at the eight adjacent nodes. Figure 2 shows the results of this process; for each node, the mean correlation value (averaged over the eight surrounding nodes) is plotted for each variable (a histogram of the correlation values is shown inside each panel). It can be seen that both temperature (Fig. 2a) and precipitation data (Fig. 2b) are highly spatially correlated within neighbor nodes in most of the domain.

The advantage of using RCMs for the analysis of extreme meteorological events is that they constitute physically-based methods providing information on the key climatic variables at reasonably high spatial and temporal resolution (Ekström et al 2005). RCM outputs have been exploited in many hydrological applications and often analysed through two principal methods: (1) the regional frequency analysis (RFA), and (2) individual grid box analysis (GBA). The RFA involves the pooling of annual maxima and generally allows a more reliable estimation of high return period events; conversely, the GBA provides more detailed information about the spatial distribution of extremes (Fowler et al 2005; Ekström et al 2005). The application of RFA was pioneered in flood frequency analysis but has been little used in climate change applications. Recently, a popular RFA method, the index flood model, has been implemented with time-varying parameters as a tool to summarize changes of extreme precipitation in RCM simulations (Hanel et al 2009). In that approach, the

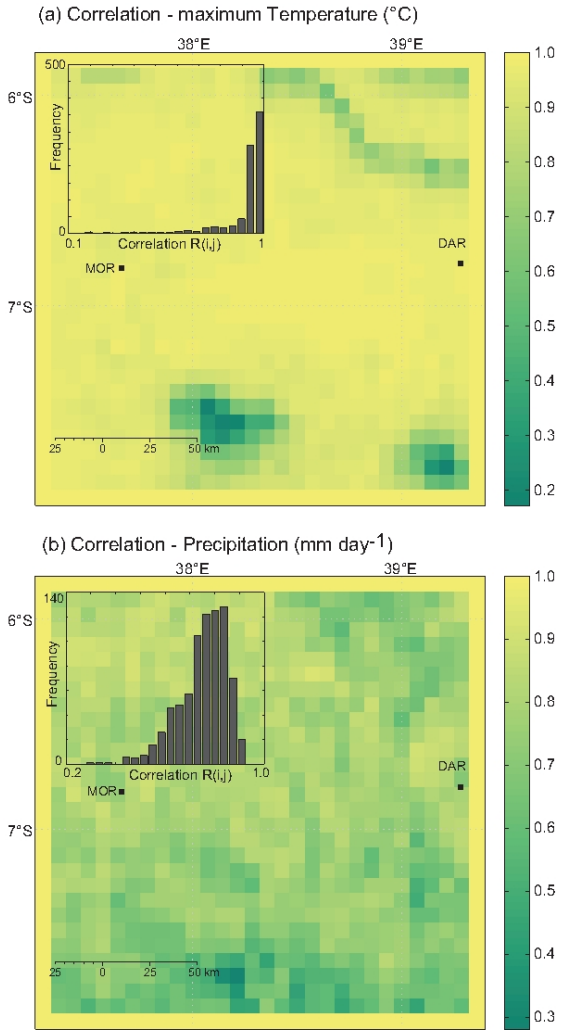

Fig. 2 Mean correlation value between the data at each node and the data from the 8 surrounding nodes for (a) temperature data, and (b) the precipitation data. For each variable, a histogram of all the correlation values is presented inside each panel.

temporal trend in the location parameter of the GEV distribution is assumed to be constant over the region of interest, which is motivated assuming that changes in extreme precipitation are mainly associated with large-scale changes in the atmospheric conditions (Hanel et al 2009). However, in some cases this assumption may not be verified, as for example in regions with steep orographic features where temperature and precipitation changes may be altitude-dependent (e.g. Giorgi et al 1997; Hanel et al 2009), or in regions covering wide areas.

The main goal of this work is to provide a high resolution tracking of spatial and temporal variations of extremes, and therefore a GBA approach has been adopted. To maximize the reliability of the results (especially for events with very low probability), rigorous approaches for both the model parameter estimation and the model selection have been implemented along with propagation of uncertainties. The procedure adopted can be summarized as follows:

1. At each node of the domain (Fig.1b), synthetic time series of the maximum daily temperature at 2 meters from the ground and the 24-hours cumulated precipitation variables were obtained from the climate simulations performed taking into account two possible climate change scenarios.
2. EV analyses considering stationary and non-stationary conditions in the GEV location parameter are performed using the annual maxima data (Section 2.1). The model parameter estimation is performed using a Bayesian approach (Section 2.3).
3. The same EV analysis is applied to the stochastically downscaled precipitation fields (Section 3.3) over a domain of about 20×20 km^2 that roughly covers the Dar es Salaam city area (Fig. 1c).
4. A procedure for model selection is applied (Section 2.4) and the 'preferred models' are used to plot the results in terms of (a) hazard curves at each node, and (b) exceedance probability maps for the whole area considering specific probability threshold values (Fig.1d).
5. In the case of non-stationarity, the plot of the temporal trend of the intensity parameter at given exceedance probability values is also shown.

2.1 GEV distribution with covariates

The generalized extreme-value distribution function (Jenkinson 1955) has the from:

$$G(z|\mu,\sigma,\xi) = \exp\left\{-\left[1+\xi\left(\frac{z-\mu}{\sigma}\right)\right]^{-1/\xi}\right\} \qquad (1)$$

where μ is the location parameter, σ is the scale parameter and ξ is the shape parameter. A detailed description of the main characteristics of the GEV family of distributions is presented in Appendix A. The Frechét (or Type II) and Weibull (or type III) classes of EV distribution correspond respectively to the cases $\xi > 0$ and $\xi < 0$ in this parameterization, whereas the special case obtained for $\xi \to 0$ is the Gumbel (or Type I) class, with distribution function:

$$G(z|\mu,\sigma,\xi) = \exp\left\{-\exp\left[-\left(\frac{z-\mu}{\sigma}\right)\right]\right\}; z \in \mathbb{R} \qquad (2)$$

Hereinafter we adopt the notation $\mathbf{z} \sim \text{GEV}(\theta)$ to denote the GEV distribution with stationary parameters represented by the vector $\theta = (\mu, \sigma, \xi)$, as presented in Eq. 1. In order to consider possible temporal trends

we adopt a pragmatic approach based on the use of the standard extreme value models as a basic template, and where possible variations through time in the observed processes are modeled writing the model parameters in terms of deterministic functions of explanatory covariates (Coles 2001). Examples of covariates that have been related to the climatological data are the time (e.g., Coles 2001; Ouarda and El-Adlouni 2011; Seidou et al 2012; Katz et al 2002) or the 'Southern Index Oscillator' (SOI, e.g., Coles 2001; El Adlouni et al 2007).

To analyze extremes of non-stationary sequences we follow the covariate approach described in Coles (2001). Since the time series available for the analyses are relatively short, the implemented model is kept simple allowing possible time dependency only in the location parameter (denoted as μ_t) and assuming σ and ξ as constant. Despite there are evidences in the literature of possible temporal changes in σ (e.g., Khaliq et al 2006; El Adlouni et al 2007), the model adopted here seems in any case reasonable in light of the results of Zhang et al (2004), who used Monte Carlo simulations to compare several methods for detecting trends in the magnitude of extreme values and suggested the advantages of using more parsimonious models. In particular, Zhang et al (2004) highlighted the problems that may arise when trends are allowed in both location and scale parameters.

The model for the data $\mathbf{z}_t$ (the annual maximum of the considered variable at time t), is therefore represented by:

$$\mathbf{z}_t \sim \text{GEV}(\theta_t), \quad \text{for } \theta_t = (\mu_t, \sigma, \xi) \tag{3}$$

where the location parameter, μ_t, can be described as:

$$\mu_t(t) = \sum_j \beta_j f_j(t) \tag{4}$$

and where $\beta = (\beta_0\ \beta_1\ \cdots\ \beta_j)'$ is a vector of parameters, and $f_0(t) = 1$ (for $j = 0$). For μ_t we test different models against the hypothesis of stationarity represented by $\mu_t \equiv \mu = \beta_0$. The considered models range from a linear trend ($j = 1$: $\mu_t(t) = \beta_0 + \beta_1 t$ in Eq. 4) to higher degree polynomials (for $j > 1, \mu_t(t) = \beta_0 + \beta_1 t + \beta_2 t^2 + \cdots$). It is worth noting that polynomials with degree > 1 always performed worse than the stationary case, and this may be due to the relatively short time series used. Therefore, the non-stationary model presented in this paper is always referred to a linear trend in μ_t.

2.2 Output information for hazard assessment

The harmonization of the output of probabilistic hazard assessment analyses is one of the first and fundamental requirements for quantitative multi-hazard and multi-risk assessments (Marzocchi et al 2012). The output of our analyses for different variables is harmonized producing results in terms of hazard maps and hazard curves. The hazard maps represent the spatial distribution of the intensity values z_p for given annual exceedance probabilities p; conversely, the 'hazard curves' represent the 'intensity value' z with the (annual) probability of exceedance of threshold values z_{th}, $p(z > z_{th})$.

$p(z > z_{th})$ can be determined using the survival function $\{1 - G(z)\}$, whereas z_p is calculated using the quantile function $G^{-1}(1 - p; \mu, \sigma, \xi)$ that is obtained inverting Equation 1 (e.g., Coles 2001):

$$\begin{aligned} z_p &= G^{-1}(1-p;\mu,\sigma,\xi) \\ &= \begin{cases} \mu - \frac{\sigma}{\xi}[1 - \{-\log(1-p)\}^{-\xi}], & for\ \xi \neq 0 \\ \mu - \sigma\log\{-\log(1-p)\}, & for\ \xi = 0 \end{cases} \end{aligned} \tag{5}$$

Finally, in the case of non-stationary conditions, another important output of interest is a plot of the temporal evolution of z_p (for a given exceedance probability value p); in this case, we use the quantile function shown in Equation 5 taking into account the time dependency of the location parameter μ_t,

$$z_p(t) = G^{-1}(1 - p; \mu_t(t), \sigma, \xi) \tag{6}$$

2.3 Parameter estimation using Bayesian inference

Methods commonly used to estimate the parameters of the non-stationary GEV model include the maximum likelihood approach (e.g. Coles 2001; Katz et al 2002), the generalized maximum likelihood approach (e.g., El Adlouni et al 2007; Cannon 2010), which uses prior information on the shape parameter ξ to eliminate potentially invalid values of this parameter, and procedures based on Bayesian inference (e.g., Coles 2001; Beaulieu et al 2008; Ouarda and El-Adlouni 2011; Seidou et al 2012). In this work, a fully Bayesian approach to parameter estimation and inference is used. Computations are performed using a Markov chain Monte Carlo (MCMC) method based on the Metropolis-Hastings algorithm (for details see Appendix B). A Bayesian method is an efficient approach for the estimation of the GEV model parameters in presence of non-stationary conditions; furthermore, it constitutes a natural framework to incorporate different sources of information and to handle uncertainties.

One of the main problems when applying a Bayesian method is to select the prior distributions in the parameter space, ($\pi(\theta)$, see Appendix B for notation). Specifying a prior distribution is a necessary component of any Bayesian analysis, even if there is no information with which to do so. In such situations it is usual to use priors that have very high variance reflecting the absence of genuine prior information. There

is considerable literature on this issue, even in the applications using the GEV distribution, and in practical terms, results are not usually sensitive to choices of prior distributions that have a sufficiently large variance (Coles 2001). However, objective problems and instabilities when performing inference on ξ parameter have been found in many hydometeorological applications, especially when small samples are analyzed (e.g., Martins and Stedinger 2000; El-Adlouni et al 2006; Ouarda and El-Adlouni 2011); therefore, the ξ is the parameter requiring more attention and a Bayesian approach can provide a reliable scheme to determine the ξ values and uncertainties.

To set the prior state of information for the σ and μ (in the stationary case) or σ and β_i (in the non-stationary case) parameters, in our analyses we always adopt 'non informative' priors defined as Normal density functions with mean zero and large variance. Conversely, for the ξ parameter we propose an analysis in two-steps: first, we perform an initial 'inference trial' in the whole domain using either non informative priors with zero mean and large variance (e.g. a Normal distribution $\mathrm{N}(\mu_\xi, \sigma_\xi)$), or testing 'poorly' informative priors with the mean μ_ξ set by using information from literature (i.e., considering ξ values obtained by other authors, or even prior distributions already proposed in literature); as in the previous case, a large variance σ_ξ^2 is used. It is worth noting that in the analyzed cases, both the non informative and the 'poorly' informative priors have had negligible effect on the posterior of ξ. Details of the specific definition of the 'poorly' informative prior distributions for ξ for the temperature and precipitation data are presented at the beginning of their respective subsections in Section 4.

The second step of the analysis is the key element of the paper and is applied when it is suggested by the results obtained in the first step. In practice, we analyze the ξ values obtained at the first step of the process for all the nodes of the domain (median value, and the 16th and 84th percentiles as uncertainty bounds) and check for the spatial coherence of the results. By spatial coherence we mean that possible spatial changes in the values are smooth, avoiding nodes with values in strong contrast with the adjacent ones. When there is a node with a ξ value in strong contrast with the ξ values obtained in the area around it (Fig. 3a and b), then we use the 'coherent' results obtained in the cloud of nodes around the node under suspect to set a more informative prior distribution $f(\mu_\xi, \sigma_\xi)$ for ξ at the node(s) with incoherent results (Fig. 3c to e). Note that as result of the analysis at the first step we obtain, at each node, an empirical probability distribution for ξ; therefore, to set the prior distribution for the analysis at the second-step, we sample the empirical distributions of ξ in the neighbor nodes (in a predefined area). Note also that, for simplicity, $f(\mu_\xi, \sigma_\xi)$ can be defined as a Normal distribution, but this is not a condition and therefore the functional form of $f()$ can be derived from the sampled values. With the information provided by the neighbor nodes encoded in the prior distribution, the second step of the analysis is done to estimate the parameter values just in the nodes with 'suspicious' (incoherent) results at the first-step (Fig. 3f).

2.4 Model selection using Bayes factors

Testing different competing models require an adequate strategy to select an appropriate model. The Bayes factor is the standard Bayesian solution to the hypothesis testing and model selection problem (e.g., Kass and Raftery 1995; Raftery 1996; Lewis and Raftery 1997b). The Bayes factor, B_{kl}, for comparing model M_k to Model M_l for observed data $\mathbf{z}$, is the ratio of the posterior odds for M_k against M_l to the prior odds. When the models M_k and M_l are equally probable a priori, then B_{kl} reduces to:

$$B_{kl} = \frac{f(\mathbf{z}|M_l)}{f(\mathbf{z}|M_k)} \tag{7}$$

Therefore, B_{kl} is the ratio of the integrated (or marginal) likelihoods of the two models being compared (Lewis and Raftery 1997b). Computing $f(\mathbf{z}|M_m)$ is rather tricky and is still topic of intense research in applied statistics. Different approaches have been proposed and applied in literature (reviews and discussions can be found in e.g., Kass and Raftery 1995; Raftery 1995; Lewis and Raftery 1997b). Because of its simplicity and easy implementation, the harmonic mean of the posterior distribution (Newton and Raftery 1994; Raftery et al 2007) is one of the most used methods to calculate Bayes factors (e.g., Seidou et al 2011, 2012); however, the sample posterior harmonic mean does not have finite variance in general and so is often unstable. Details about this issue can be found in Newton and Raftery (1994) and Raftery et al (2007).

To estimate the marginal likelihoods for the Bayes factor calculation we have implemented the Laplace-Metropolis estimator (Raftery 1996; Lewis and Raftery 1997a), which uses the posterior simulation output to estimate the integrated likelihoods. A detailed description of the method used here is presented in Appendix C (and references therein).

The Bayes factor can be interpreted as a summary of the evidence provided by the data in favor of one specific model as opposed to another. Jeffreys (1961) suggested interpreting B_{kl} in half units on the $\log_{10}$ scale

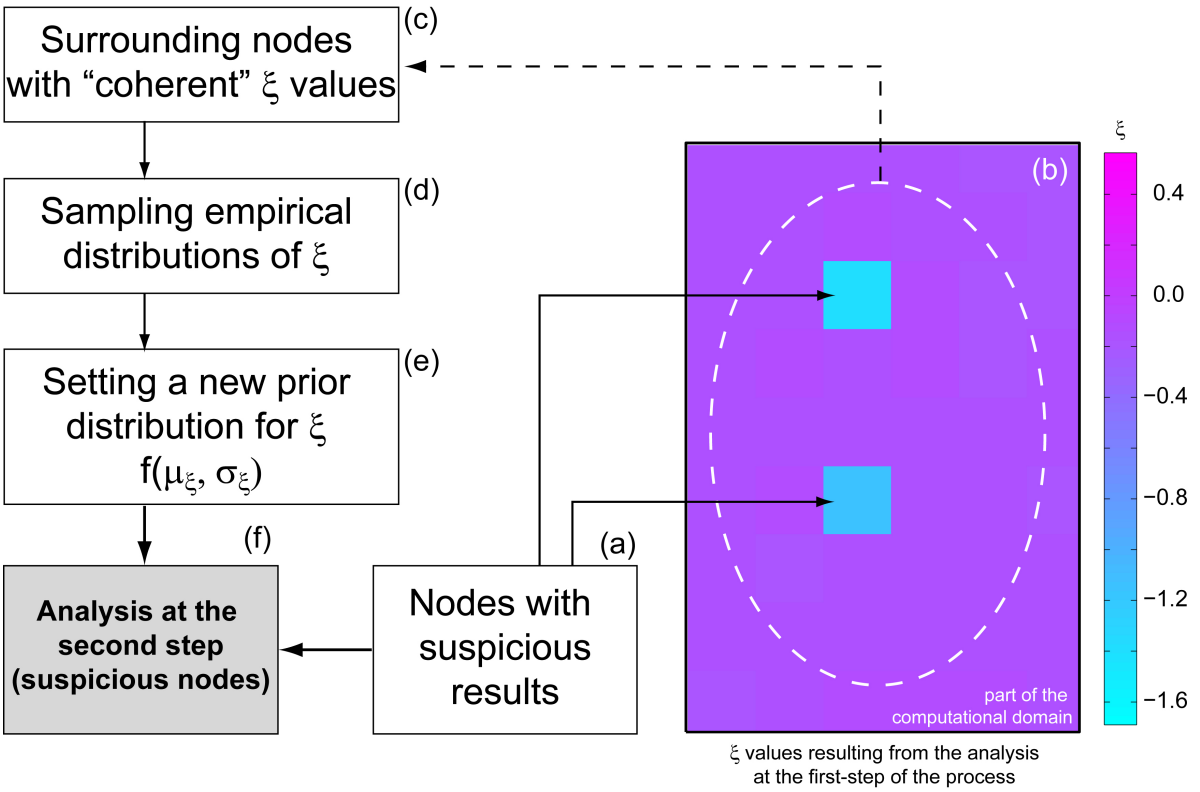

Fig. 3 Description of the two-steps inference process for the definition of the prior information of the ξ parameter.

Table 1 Categories used as reference for the interpretation of the Bayes factors B_{kl} for the model selection, as presented in Raftery (1996) and modified from Jeffreys (1961)

$2\log_{10}(B_{kl})$	B_{kl}	Evidence for M_k
< 0	< 1	negative (supports M_l)
0 to 2	1 to 3	barely worth mentioning
2 to 5	3 to 12	positive
5 to 10	12 to 150	Strong
> 10	> 150	very strong

and proposed different categories to assess the evidence against the reference model M_k. Here, for the model selection and interpretation of results we adopt the categories proposed by Raftery (1996) as shown in Table 1, which is slightly modified from the initial proposal of Jeffreys (1961). In this case, it is suggested to consider twice the logarithm of the Bayes factor, which is on the same scale as the familiar deviance and likelihood-ratio test statistics.

3 Data

3.1 Climate simulations

Climate projections in response to increasing greenhouse gases concentrations are usually evaluated using GCMs. They are characterized by spatial resolutions generally around or coarser than 100×100 km. On the other hand, RCMs with higher horizontal resolution are usually nested into GCMs to provide a more detailed description of the climate variability at the regional and local scales and therefore they are used to perform impact studies (Bucchignani et al 2013). A RCM is generally able to take into account elements like mountains, coastlines and changing vegetation, representing in a better way their effects on the weather. Such a precision implies a much heavier computational cost; therefore the model is limited to a restricted domain with the GCM data used as lateral boundary conditions (dynamical downscaling).

In this work, we analyse the output of the non-hydrostatic COSMO-CLM climate model (COSMO-CLM, Rockel et al 2008), the climate version of the COSMO local model (COSMO-LM, Steppeler et al 2003). The development of COSMO-CLM has been driven by two main reasons: the first was the idea of developing a model able to simulate both weather and climate, and the second was the need of introducing a non-hydrostatic formulation, in order to have a convection resolving weather simulation. This is a very important topic, due to the difficulty in predicting the effects of this phenomenon, such as sudden high intensity precipitation. COSMO-CLM can be used with a spatial resolution

between 1 and 50 km even if the non-hydrostatic formulation of the dynamical equations in CLM made it eligible especially for the use at horizontal grid resolution lower than 20 km (Bohm et al 2006) and therefore closer to the requested resolution for impact modeling.

3.2 Climate projections over Dar es Salaam area

The climate projections have been obtained forcing COSMO-CLM with the output of the global model of the 'Centro Euromediterraneo sui Cambiamenti Climatici' (CMCC, Gualdi et al 2013) considering the domain shown in Fig. 1a and covering the time period 1950-2050. The simulations have been performed at a spatial resolution of 8 km, with 40 vertical levels, and with a temporal resolution of 50 sec. In the period 1950 to 2005, the climate simulations use data from regional observations for a quality check of the model results and to optimize the model configuration, reducing in this way the bias affecting the simulation output (Bellprat et al 2012). Future climate is analyzed for two Representative Concentration Pathways (RCP) scenarios RCP 4.5 and RCP 8.5 (Moss et al 2010; IPCC 2013), where the numbers 4.5 and 8.5 indicate the anthropogenic radiative forcing in 2100 relative to a pre-industrial period (1850).

The output of the climate projections have been first analyzed comparing the average values of temperature and precipitation over the time period 2021-2050 (both the scenarios) with the average values over the time period 1971-2000. Fig. 4 shows the changes in the 2-meter temperature (t2m) for the period December-January-February (DJF, Figs. 4a and 4c) and June-July-August (JJA, Figs. 4b and 4d). The figures in the top row are from the RCP4.5 scenario, and those in the bottom row are from the RCP8.5 scenario. In the RCP4.5 scenario, the temperature changes are expected to be in the range from 1°C to 1.5°C, with the lowest values along the coast and no substantial seasonal differences (minimum values are slightly higher in JJA than in DJF). The spatial distribution of the expected changes in the RCP8.5 scenario, as shown in Fig. 4c and 4d, do not differ too much with respect to the other scenario, yet they are slightly higher: also here, values rise by moving into the internal area with a range of 1.2°C to 1.6°C in DJF and 1.4°C to 1.7°C in JJA. Figure 4 (e to h) shows also the precipitation results (percentage change) considering both scenarios (RCP4.5 in the top row and RCP8.5 in the bottom row). In DJF, there is a significant percentage reduction in the internal area, with peaks of -40%, while the trend is inverted approaching to the coastal line (up to +35%). A similar behavior is observed considering the RCP8.5 scenario, nevertheless it features less intense changes. Furthermore, no significant variations are registered in JJA (+/-5% for both scenarios).

3.3 Stochastic precipitation downscaling

For many hydrological applications and impact studies in urban areas, a further downscaling of the climate information produced by RCMs is often required (Sorooshian et al 2008). Stochastic downscaling procedures represent a possible approach to generate realizations of small-scale precipitation fields. In recent years, several stochastic downscaling techniques have been proposed to generate high-resolution precipitation, including point-process models (Waymire et al 1984), fractal cascades (Lovejoy and Mandelbrot 1985; Perica and Foufoula-Georgiou 1996; Menabde et al 1997) and autoregressive models (Bell 1987). Regardless of the specific approach, the stochastic downscaling methods are able to generate variability at the scales not resolved by the physical, dynamically-based models and permit the creation of large ensembles of synthetic fields, also at very high spatial and temporal resolutions, allowing for the evaluation of the probabilities of occurrence of intense and localized precipitation events over small areas.

In this work we have applied a stochastic rainfall downscaling procedure called RainFARM (Rainfall Filtered Autoregressive Model, Rebora et al 2006a,b) able to generate small-scale precipitation fields by propagating the statistical properties of larger-scale fields (such as the shape of the power spectra) to small scales. The model version employed in this study is particularly suitable to perform purely spatial downscaling for applications on climatological time scales (e.g., to the output of RCMs, D'Onofrio et al 2014). We have used RainFARM to perform a purely spatial downscaling of the daily precipitation fields generated by COSMO-CLM, obtaining new precipitation data with a spatial resolution of 1×1 km. We focus on a small area around the Dar es Salaam city, ranging from 39.14°E to 39.31°E longitude and from −6.76°S to −6.93°S latitude, as shown in Figure 1c. We have downscaled the precipitation simulated by COSMO-CLM for both the historical period (1980-2005) and for the future decades (2006-2050) under both emission scenarios (RCP4.5 and RCP8.5).

4 Results

Following the structure of the climate simulations, the data has been divided in two time periods: a 'historical period' which comprises the data between 1950 and

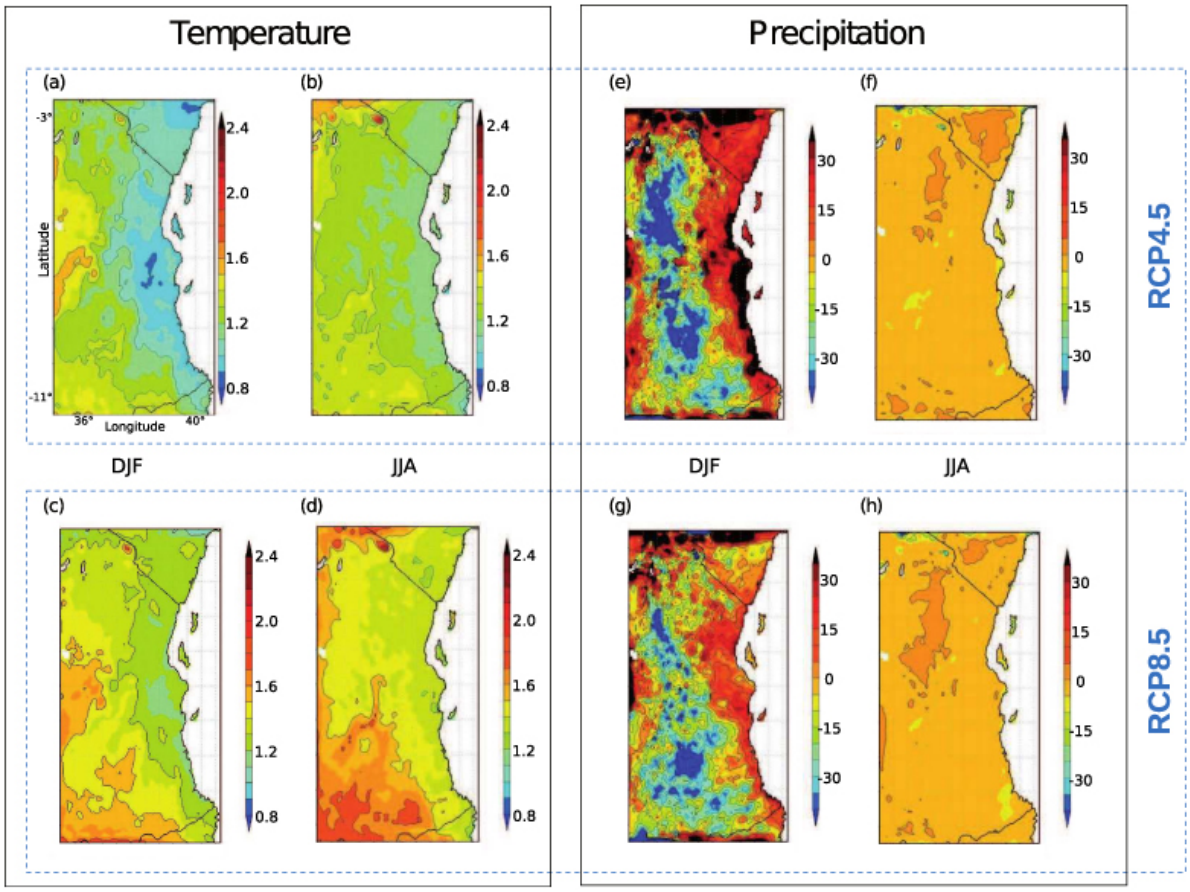

Fig. 4 Seasonal changes of mean temperature at 2 meters from ground (a to d, in °C) and Percentage change of seasonal precipitation (e to h) for the time period 2021-2050 with respect to 1971-2000. The figure shows the plots for two seasons: DJF and JJA. The first row shows the results considering the RCP4.5 scenario, and the second row the results considering the RCP8.5 scenario.

2005, and a 'projection period', which comprises the data between 2006 and 2050. Figure 5 shows examples of annual maximum temperature (Fig. 5a) and 24-hours cumulated precipitation (Fig. 5b) of the daily data in a single node located in the area of the Dar es Salaam city ($X = 39.2471°$ latitude; $Y = -6.8355°$ longitude); in all the panels the red circles represent data in the historical period, and the blue triangles and yellow squares represent the data in the projection period considering, respectively, the RCP4.5 and RCP8.5 scenarios. The procedure described in Section 2 has been used to analyse the temperature and precipitation data and this section summarizes the obtained results.

4.1 Extreme temperature

When treating temperature data, it is possible to analyze it in terms of extreme temperature (as e.g., in Siliverstovs et al 2010; Scotto et al 2011; Hrafnkelsson et al 2012), or in terms of prolonged (in time) extreme temperature events (usually referred to as heat waves or cold spells, e.g., Huth et al 2000; Kysely 2002, 2010). Extreme value distributions often provide unstable results when applied to maximum annual lengths of heat waves, but it is considered probably the best method for annual one-day temperature extremes (Kysely 2002). In this section we analyze the maximum daily temperature data, without considering the heat wave events.

Using the Bayesian approach described in Section 2.3, first we have defined a non informative prior for ξ, set as $\xi \sim N(\mu_\xi = 0, \sigma_\xi^2 = 100^2)$. Different tests were also performed defining 'poorly' informative prior distribution for ξ considering the results presented by different authors analyzing temperature data (e.g., Siliverstovs et al 2010; Scotto et al 2011; Hrafnkelsson et al 2012); in this case we set $\mu_\xi = -0.229$, whereas for the variance we tested different values: 100^2 as in the previous case, 10^2, and 3^2, the last value resulting wide enough to describe the variability found in literature. The effects of these priors on the results were completely negligible. The second step of the inference process was applied to different nodes of the domain show-

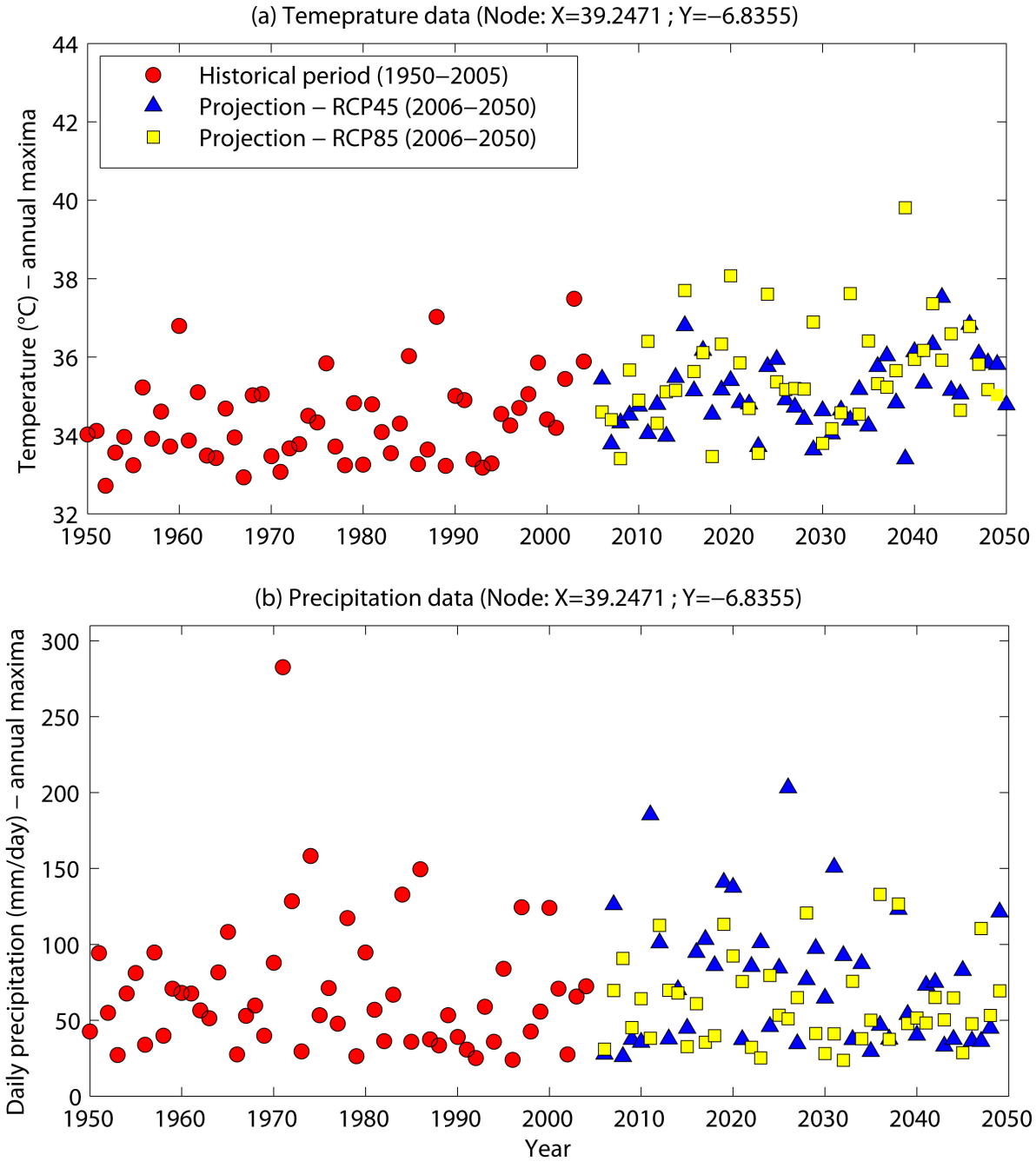

Fig. 5 Annual maxima of temperature and daily precipitation in a single node located close to the Dar es Salaam city (latitude 39.2471°, longitude −6.8355°): (a) annual maxima in the 2-meter temperature; (b) annual maximum daily precipitation. The red circles represent the data in the historical period (1950-2050), whereas the blue triangles and the yellow squares represent the data in the projection period (2006-2050) considering, respectively, the RCP4.5 and RCP8.5 scenarios.

ing results contrasting with the average values of the neighbor nodes. In those cases, more informative priors using the information from the neighbor nodes have been set.

To select the preferred models, the Bayes factor B_{10} was calculated to confront the non-stationary, linear trend model in μ_t (M_1) with the stationary case (M_0). Fig. 6a show the spatial distribution of the calculated B_{10} for the historical period, and Figs. 6b and 6c the B_{10} for the projection period considering, respectively, the RCP4.5 and the RCP8.5 scenarios. A flat surface representing the values $\log(B_{10}) = 0$ has been included to mark the limit between the values in which the stationary case (M_0) is the preferred model (i.e., $\log(B_{10}) \leq 0$), and those in which there is evidence against M_0 (i.e., $\log(B_{10}) > 0$), in a measure as repre-

sented in Table 1. For the historical period, the stationary model results the preferred model in the whole domain (Fig. 6a). Likewise, for the projection period with the RCP4.5 scenario, the stationary model is preferred in most of the surface except for an area located at the NE of the domain, where the linear trend in μ_t is the preferred model (Fig. 6b). This area corresponds with a sea strip in our domain located between the continent and the Zanzibar Island. Finally, for the projection period with the RCP8.5 scenario, the linear trend in μ_t is the preferred model in practically the whole domain (Fig 6c).

Figs. 6d, 6e and 6f show histograms of the ξ values obtained, respectively, for the historical period, the RCP4.5 and the RCP8.5 scenarios (the 50^{th} percentiles as 'best values', and the 16^{th} and 84^{th} percentiles representing uncertainty bounds). The inner plot in each panel shows the spatial distribution of the 50^{th} percentile of ξ. These figures represent the results obtained after the inference analysis at the second step; in contrast with what happens with the precipitation data, a non negligible number of nodes keep their contrasting results (see e.g. the case for the RCP4.5 scenario in Fig. 6d). In these cases the informative priors do not influence the posterior and therefore, being of difficult physical interpretation, these nodes with inconsistent results are considered as 'noise' in our solutions. Most of the solutions are characterized by $\xi < 0$; in fact, we find that the mean of the ξ values in the whole domain (using the 50^{th} percentile from each node and excluding those considered as noise) is $-1.1 \times 10^{-1}(\pm 8.7 \times 10^{-2})$ in the historical period, $-1.61 \times 10^{-1}(\pm 6.9 \times 10^{-2})$ in the projection period with the RCP4.5 scenario, and $-1.68 \times 10^{-1}(\pm 5.5 \times 10^{-2})$ in the projection period with the RCP8.5 scenario. It indicates that the upper-side bounded Weibull is the dominating distribution of the GEV family for the temperature data. We note also that the mean value of ξ for the whole domain is significantly lower in the projection period (for both scenarios) respect to the mean value obtained for the historical period (using a t-test, the null hypothesis of equal mean is rejected at a significance level of 0.01).

The preferred models were used to create the hazard maps representing the extreme temperature values (z_p, in °C) for given exceedance probabilities p of interest (Eq. 5); likewise, the extreme temperature hazard curves were created for each node of the domain. As examples, Figs. 7a and 7b show the hazard maps of extreme temperature with exceedance probabilities of 10% and 1%, respectively. From these maps we note that, for a fixed exceedance probability value, the areas over the Sea (NE and SE of the domain) show the lower values of extreme temperature; the temperature extremes increase as moving towards the inland area, corresponding roughly with the valleys of the Ruvu and Wami rivers. Another area with lower temperature extremes is identified in the SW part of the domain, which is roughly correlated with the Uluguru Mountains (South of Morogoro), and the Pugu Hills (at the SW of Dar es Salaam). Two examples of hazard curves are represented in Fig. 7c (for the Dar es Salaam area), and 7d (for the Morogoro area). Each figure shows the 50^{th} percentile as the best value, and the 16^{th} and 84^{th} percentiles as uncertainty bounds. These uncertainties are calculated propagating the uncertainties in the values of model parameters.

In the areas where the preferred model is non-stationary, it is also of interest to plot the temporal trend of the temperature for given exceedance probability values. As seen in Fig. 6, non-stationary conditions for the temperature data are identified just in the projection period. Figure 8 shows the values of the 50^{th} percentile of the slope (β_1) at each node of the grid for the data considering the RCP4.5 (Fig. 8a) and the RCP8.5 (Fig. 8b) scenarios. The nodes in which the stationary is the preferred model, the slope $\beta_1 = 0$. Uncertainty bounds in β_1, represented by the 16^{th} and 84^{th} percentiles of their empirical distribution, are shown, respectively, in Figs. $8a_1$ and $8a_2$ for the RCP4.5 scenario, and $8b_1$ and $8b_2$ for the RCP8.5 scenario. In the inland area just the RCP8.5 scenario shows a prevalence of non-stationary conditions, with β_1 ranging from roughly ~ 0.05 to ~ 0.16°C/year. The higher values of β_1 are mainly concentrated in the central part of the domain and towards the SW of Dar es Salaam city (more or less in the area of Pugu Hills). As example, Figure 8c shows the resulting trend in temperature for a node close to Dar es Salaam city; it shows the extreme temperature trend for exceedance probability values of 10% (red circles) and 1% (black triangles). The solid lines represent the median values, whereas the shadowed areas are the uncertainty bounds defined by the 16^{th} and 84^{th} percentiles. In Section 5 we discuss the significance of these variations.

4.2 Extreme Precipitation

Quantification of precipitation extremes has different potential interests, as for example in flood hazard analyses or to elaborate agricultural or hydraulic engineering projects. As for the temperature data, first we have performed the inference at the first step defining 'poorly' informative prior distributions of ξ set as $\xi \sim N(\mu_\xi, \sigma_\xi)$. In this case, μ_ξ is defined considering the results presented by different authors analyzing daily precipitation

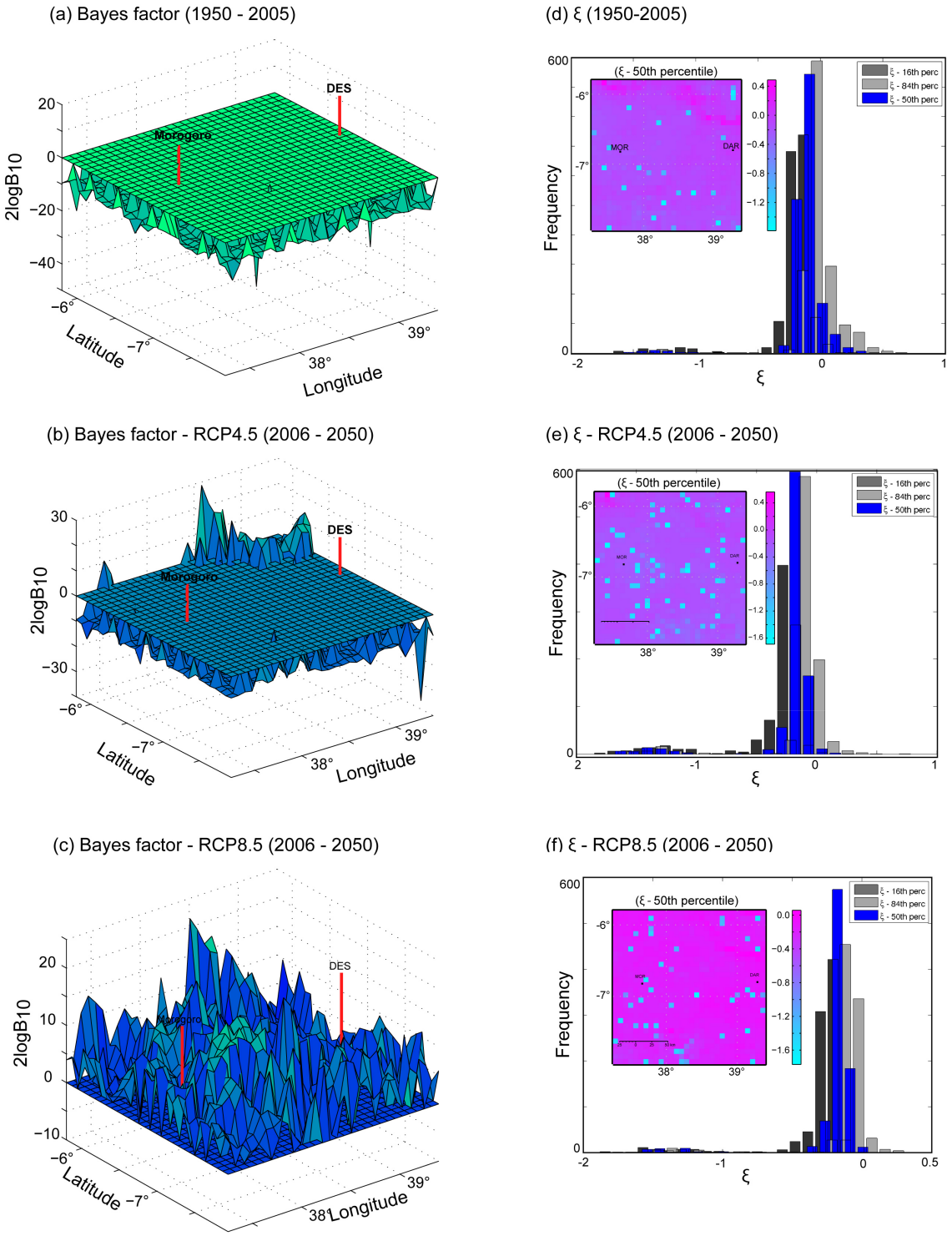

Fig. 6 First column: Spatial distribution of the Bayes factor ($2\log B_{10}$ values) calculated for the model selection considering the annual maxima in the 2-meter temperature for (a) the historical period 1950-2005, and the projection 2006-2050 period considering (b) the RCP4.5 and (c) the RCP8.5 scenarios. Second column: Histogram and spatial distribution of the ξ parameter of the GEV considering annual maxima in the 2-meter temperature for (d) the historical period, and the projection period considering (e) the RCP4.5 and (f) the RCP8.5 scenarios.

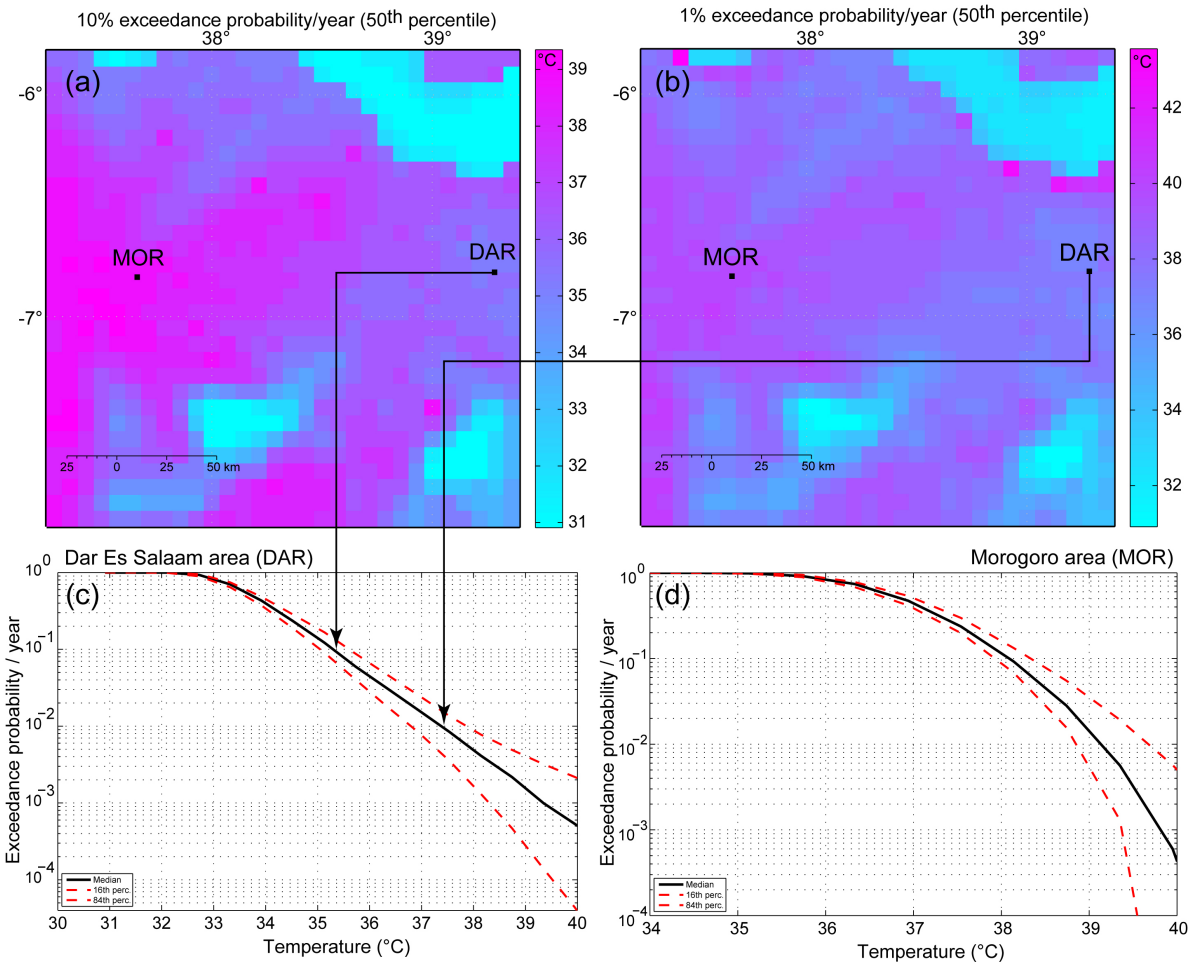

Fig. 7 Hazard maps of extreme temperature with exceedance probabilities of (a) 10% and (b) 1%, considering the data from the historical period (1950-2005). Examples of hazard curves for extreme temperature are presented for a node in (c) the Dar es Salaam area, and (d) in the Morogoro area.

data in different regions around the word. In particular, different tests were performed assuming $\mu_\xi = 0.10$ and $\mu_\xi = 0.15$; the first value, that is also in agreement with the mean of the prior for ξ proposed by Martins and Stedinger (2000) for extreme floods, is the mean value obtained from different precipitation data analyses presented in literature (i.e., Katz et al 2002; El Adlouni et al 2007; Ouarda and El-Adlouni 2011); the second value was proposed by Koutsoyiannis (2004) after analyzing 169 rainfall series from stations in Europe and in the USA. In all the cases, large variances of $100^2, 10^2$ and 3^2 were considered. The results obtained do not show substantial differences by changing the configuration of the prior distribution of ξ. The second-step analysis was applied in the nodes showing incoherent results (respect to the neighbor nodes); in these cases, more informative priors were used adopting Normal distributions with the parameters determined using the information from the neighbor nodes.

The Bayes factor B_{10} was computed to confront the non-stationary, linear trend model in μ_t (M_1) with the stationary case (M_0). The spatial distribution of the resulting values is presented in Figs. 9a, 9b and 9c, respectively, for the historical period, the RCP4.5 and the RCP8.5 scenarios. Again, a flat surface representing the values $\log(B_{10}) = 0$ has been included to mark the limit between the values in which the stationary case is the preferred model ($\log(B_{10}) \leq 0$) and those in which there is any evidence against M_0. The stationary is the preferred model in most of the area in both the historical period (Fig. 9a) and the RCP8.5 scenario data (Fig. 9e); zones with non-stationary solutions are grouped mainly in the Northern (N) part of the domain, around Dar es Salaam city, and towards the South (S). Conversely, a higher number of nodes show the non-stationary as the preferred model in the RCP4.5 scenario data, with Bayes factors reflecting positive to very strong evidence. These nodes are distributed covering a wide area, with higher density of nodes in the central part of the do-

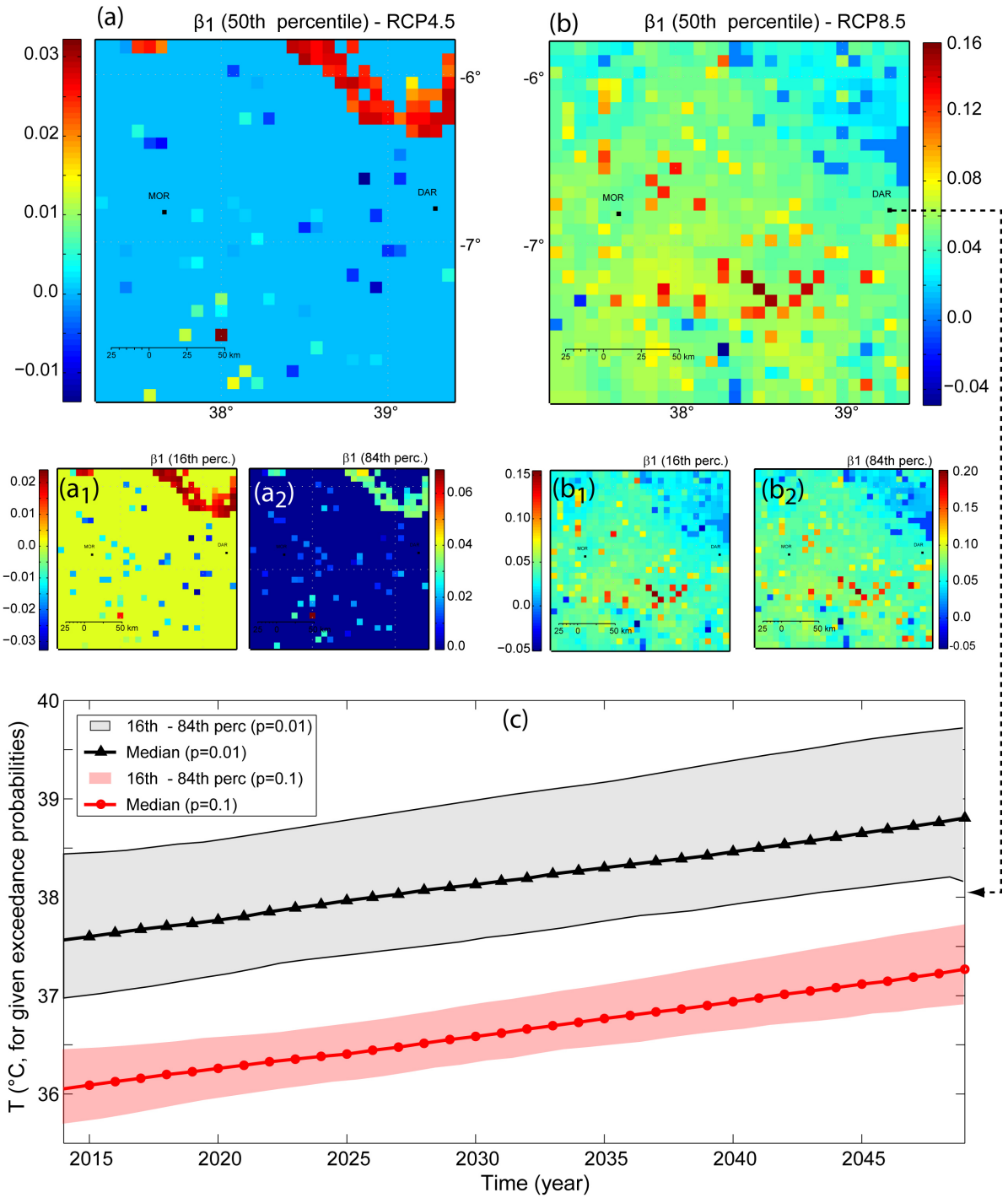

Fig. 8 Map of the 50^{th} percentile of the β_1 value for the extreme temperature data at each node of the grid for (a) the RCP4.5 and (b) RCP8.5 scenarios; uncertainties in β_1 are represented by the 16^{th} and 84^{th} percentiles (a_1 and a_2 for scenario RCP4.5, and b_1 and b_2 for scenario RCP8.5). (c) Example of the trend in the extreme temperature for values with exceedance probabilities of 1% (solid line with black triangle marks) and 10% (solid line with red circles) in the area of Dar es Salaam city and considering the RCP8.5 scenario.

main. Figures 9d, 9e and 9f show the ξ values obtained, respectively, for the historical period, the RCP4.5 and the RCP8.5 scenarios. Each panel shows a histogram with the ξ values obtained in the whole area (the 50^{th} percentiles as 'best values', and the 16^{th} and 84^{th} percentiles representing uncertainty bounds); likewise, the inner plots show the spatial distribution of the 50^{th} percentile of ξ.

From Fig. 9 it results evident that most of the solutions are characterized by $\xi \geq 0$; the mean of the 50^{th} percentiles of the ξ values in the whole domain is $6.5 \times 10^{-2}(\pm 1.5 \times 10^{-1})$ in the historical period, $7.9 \times 10^{-2}(\pm 1.7 \times 10^{-1})$ in the projection period considering the RCP4.5 scenario, and $6.5 \times 10^{-2}(\pm 1.5 \times 10^{-1})$ in the projection period considering the RCP8.5 scenario. It indicates that the Frechét (Type II) is the dominating distribution of the GEV family for the precipitation data. Most of the nodes in the domain are characterized by $0 \leq \xi \leq 0.2$; areas showing higher ξ values (ranging from 0.3 to 0.6) are concentrated, for the historical period and RCP8.5 scenario, in regions in the N part of the domain and around Dar es Salaam city (Fig. 9d and 9f, respectively), whereas for the RCP4.5 scenario these are distributed in a relatively wider area mainly located in the central and N part of the domain (Figure 9e).

Figs. 10a and 10b show the hazard maps of extreme daily precipitation with exceedance probabilities of 10% and 1%, respectively, as of 2005. From these maps we note that, for a fixed exceedance probability value, the areas showing higher extreme precipitation intensities are located (1) in the SW part of the domain, more or less covering the downstream of the Uluguru Mountains, (2) in the S of Dar es Salaam, and (3) in the NNE area of the domain (towards Zanzibar Island). For each node of the domain it is possible to obtain the extreme daily precipitation hazard curve. Hazard curve examples are represented in Fig. 10c (for the Dar es Salaam area), and 10d (for the Morogoro area). Each hazard curve plot shows the 50^{th} percentile as the best value, and the 16^{th} and 84^{th} percentiles as uncertainty bounds.

To identify the areas characterized by the more intense non-stationary conditions, Figs. 11 and 12 show the map with the values of the slope of the linear trend of μ_t (β_1 in Eq. 4) for the historical and the projection (both scenarios) periods, respectively. The 50^{th}, 16^{th}, and 84^{th} percentiles of β_1 are presented for each dataset. The nodes in which the stationary is the preferred model, the slope $\beta_1 = 0$. Comparing the β_1 values shown in Figures 11 and 12, some important differences between the historical and the projection periods emerge. First, a great number of the nodes with $\beta_1 \neq 0$ in the historical period are characterized by a negative slope ($\beta_1 < 0$) (see Fig. 11), indicating a temporal reduction in the intensity of precipitation extremes (for a given exceedance probability). Considering the median of the β_1 values, the reduction in extreme precipitation in these areas is in the order of -4 to -16 mm in 40 years. Conversely, considering the projection period, this feature is just evident in some nodes towards the NNW of the domain, whereas in the S of the domain β_1 is mostly positive, indicating a temporal increase in the intensity of precipitation extremes. Considering the areas with $\beta_1 < 0$ in the projection period, the reduction in precipitation in the NW of Dar es Salaam is of the same order of magnitude as that observed for the historical period (-4 to -16 mm in 40 years), with peak values at the N of Dar es Salaam counting with a reduction of -12 to -24 mm in 40 years. Considering instead the nodes with $\beta_1 > 0$, they are pointing to an increase in precipitation intensity in the order of 24 to 48 mm in 40 years.

Fig. 12c shows the resulting trend in extreme daily precipitation in a node located in the S part of the domain and considering the RCP8.5 scenario. The selected example represents one of the areas with the higher slope in the linear trend. The plot in Fig. 12c presents the resulting extremes with exceedance probabilities of 10% (red circles) and 1% (black triangles). The solid lines are the median values and the shadowed areas are the uncertainty bounds (16^{th} and 84^{th} percentiles). The differences in the precipitation extremes between 2013 and 2050 are more robustly analyzed considering both the median values and the uncertainty bounds. This issue is discussed in Section 5.

4.3 High resolution precipitation extremes

Using the stochastic downscaling procedure described in Section 3.3 we have generated an ensemble of rainfall realizations by considering uncertainties in the few free parameters of the RainFARM procedure, namely the spatial scale at which the original data are considered reliable, and the logarithmic slope used to extrapolate the spatial power spectra of the original model data to the small scales (D'Onofrio et al 2014).

The results of the EV analyses applied to the downscaled precipitation field data for the RCP4.5 scenario are presented in Fig. 13. The plot of the spatial distribution of the Bayes factor in the domain of the downscaled data is presented in Fig. 13a; as in the previous cases, a flat surface representing the values $\log(B_{10}) = 0$ has been included to mark the limit between the values in which the stationary case (M_0) is the preferred

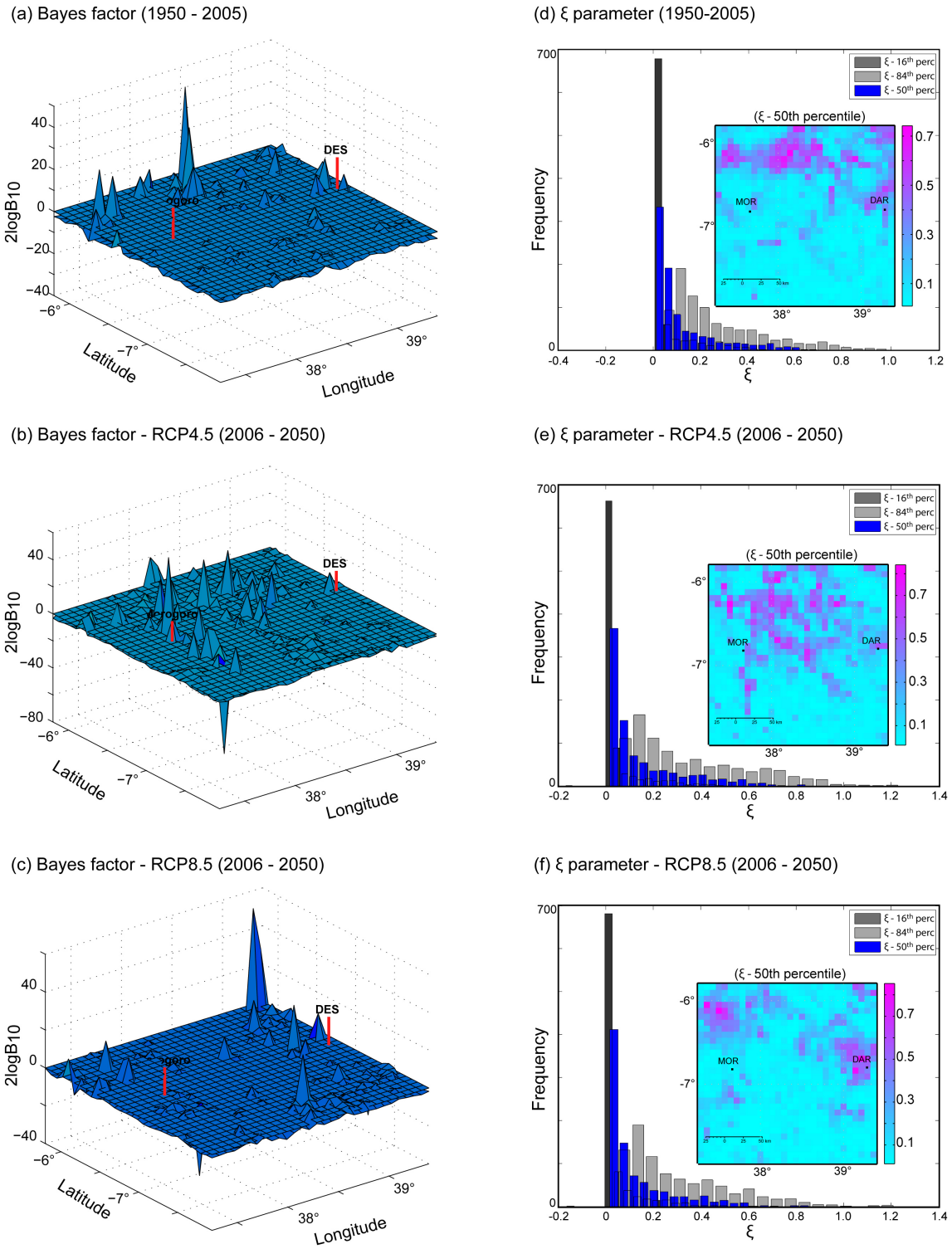

Fig. 9 First column: Spatial distribution of the Bayes factor ($2\log B_{10}$ values) calculated for the model selection considering the annual maximum daily precipitation for (a) the historical period 1950-2005, and the projection 2006-2050 period considering (b) the RCP4.5 and (c) the RCP8.5 scenarios. Second column: Histogram and spatial distribution of the ξ parameter of the GEV considering the annual maximum daily precipitation for (d) the historical period, and the projection period considering (e) the RCP4.5 and (f) the RCP8.5 scenarios.

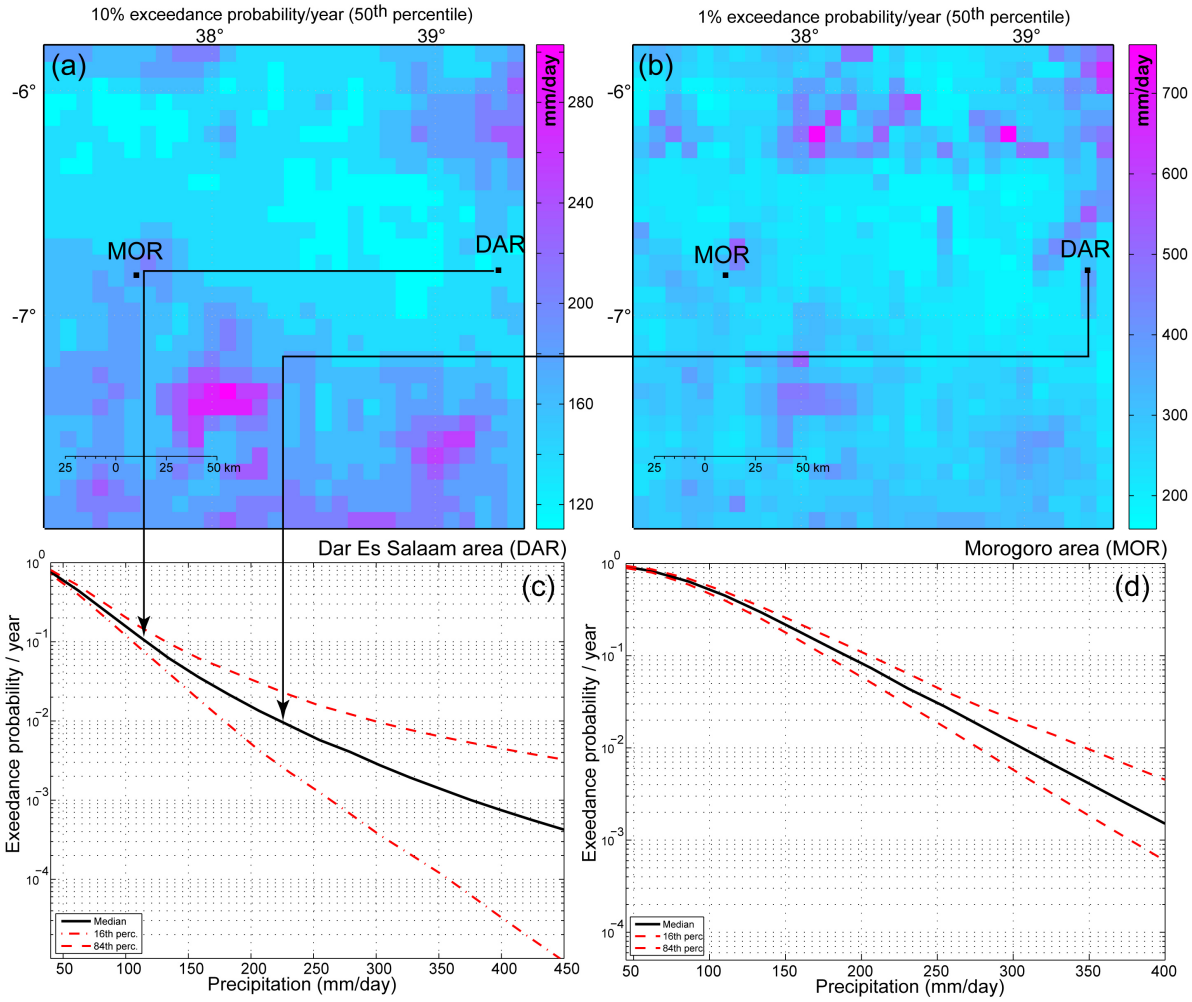

Fig. 10 Hazard maps of extreme daily precipitation with exceedance probabilities of (a) 10% and (b) 1%, considering the data from the historical period (1950-2005). The map represents the values as of the year 2005. Examples of hazard curves for extreme daily precipitation are presented for a node (c) in the Dar es Salaam area, and (d) in the Morogoro area.

model and those in which there is evidence against M_0. For reference, Fig. 13b shows the plot of 1% exceedance probability hazard map as of 2005 obtained form the original data (as in Fig. 10); the box inside this map shows the area selected for the high resolution EV analysis of precipitation extremes. Fig. 13c shows the spatial distribution of the slope of the linear trend of μ_t (β_1). Non-stationary conditions are identified in an area covering the central part of the domain and are characterized by positive β_1 values, in concordance with what is shown in Fig. 12a at a lower resolution. In many nodes of the higher resolution map, the median values of β_1 are greater than the median values observed for the same area with the 8×8 km resolution data; nevertheless, these values are comprised within the uncertainty range of the values obtained from the lower resolution RCM data. Fig. 13d shows an example of the high resolution precipitation hazard map (50^{th} percentile for values with exceedance probability of 1%) as of 2006; the areas with the higher intensities in extreme precipitation are mainly located in the S part of the domain and towards the coast. Finally, an example of the hazard curve for a node close to the Dar es Salaam international Airport (point 'Airport' in Fig. 13d) is shown in Fig. 13e; the solid line is the 50^{th} percentile (as best parameter value) whereas the uncertainty bounds are represented by the discontinuous lines showing the 16^{th} and 84^{th} percentiles. Note that in this case the uncertainty bounds come from considering the uncertainties in both the parameter estimation and the data generated by the stochastic downscaling procedure. The results obtained with the downscaled data considering the RCP8.5 scenario are also coherent with the values obtained using the 8×8 km resolution data (not presented because of space limitations).

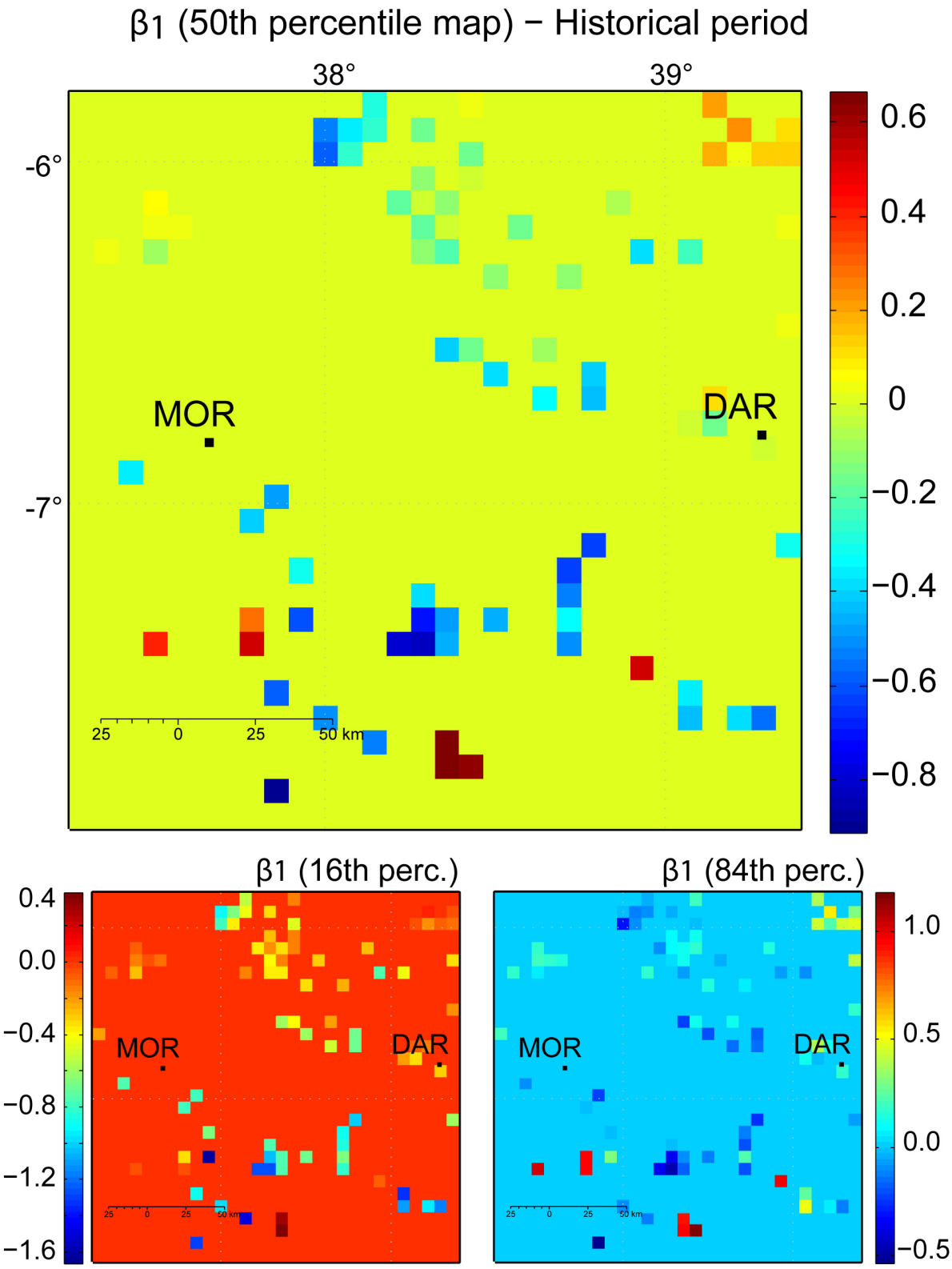

Fig. 11 (a) Map of the 50^{th} percentile of the β_1 value for the extreme daily precipitation data at each node of the grid for the historical period; uncertainties in β_1 are represented by the (b) 16^{th} and (c) 84^{th} percentiles

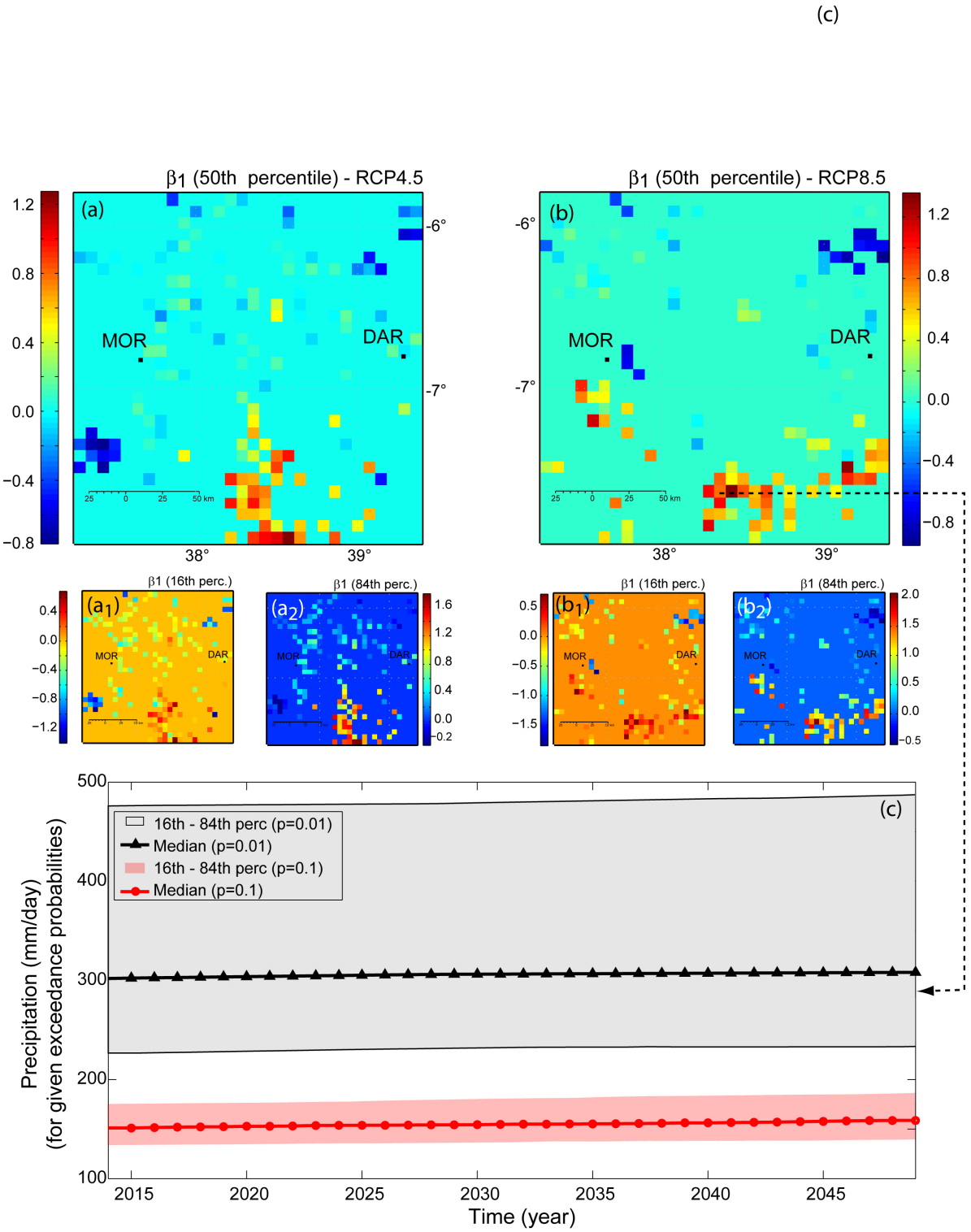

Fig. 12 Map of the 50th percentile of the β_1 value for the extreme daily precipitation data at each node of the grid for (a) the RCP4.5 and (b) RCP8.5 scenario; uncertainties in β_1 are represented by the 16th and 84th percentiles (respectively, a_1 and a_2 for scenario RCP4.5, and b_1 and b_2 for scenario RCP8.5); (c) Example of the trend in extreme daily precipitation with exceedance probabilities of 1% (solid line with black triangle marks) and 10% (solid line with red circles) in the Southern part of the domain and considering the RCP8.5 scenario.

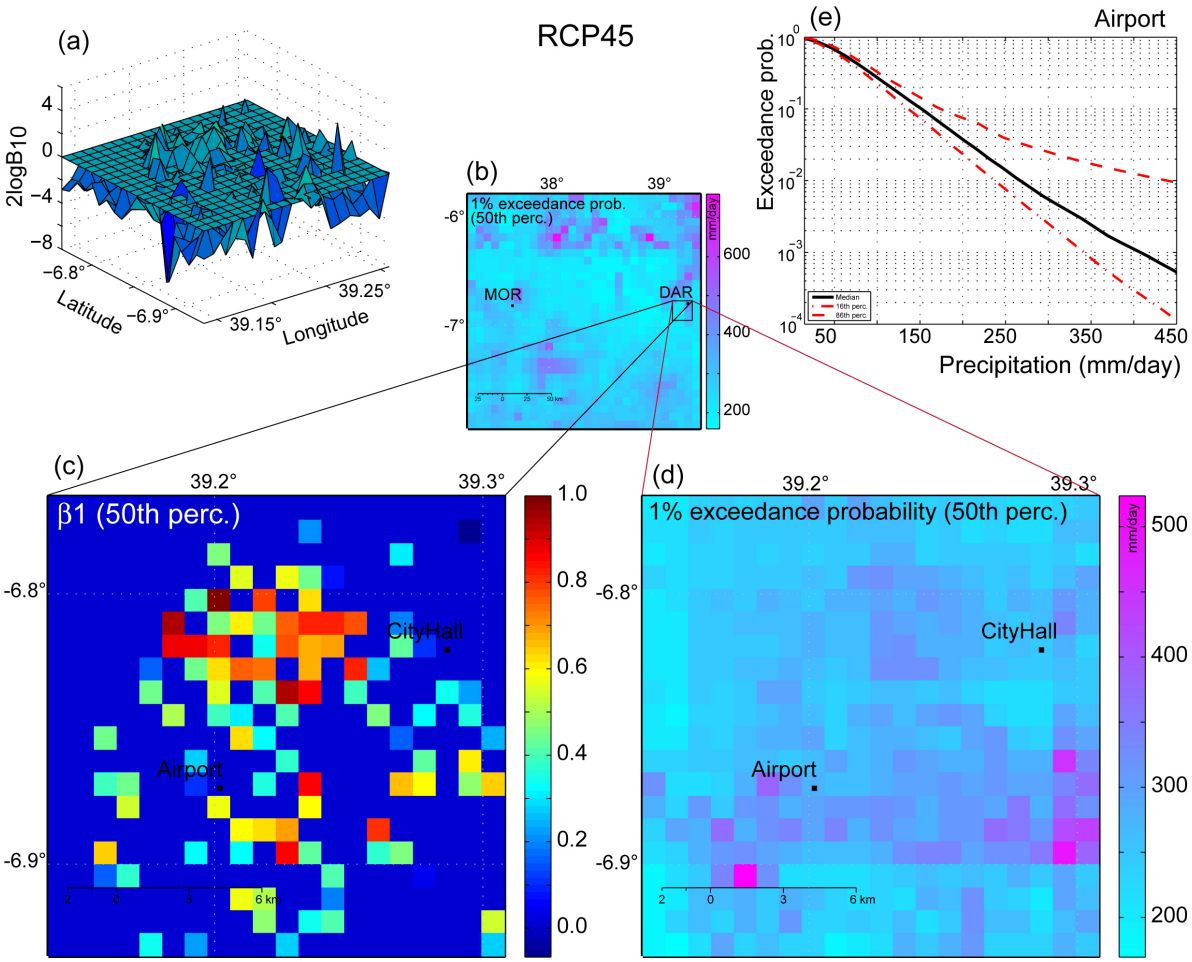

Fig. 13 Results obtained analyzing the precipitation field around Dar es Salaam city after the stochastic downscaling process, and considering the RCP4.5 scenario (projection period 2006-2050). (a) Spatial distribution of the Bayes factor; (b) Reference hazard map at 8×8 km resolution (precipitation with 1% exceedance probability). (c) Distribution of the slope (β_1 parameter) of the linear trend of the location parameter μ_t. (d) Example of the high resolution hazard map (1×1 km resolution) representing the precipitation intensity with 1% exceedance probability. (e) Example of the precipitation hazard curve for a point ('Airport') located close to the International airport of Dar es Salaam.

5 Discussion and conclusions

The non-stationary GEV model constitutes an efficient and easy-to-implement tool to take into account the dependencies between extreme events and the temporal evolution of the climate. Such a kind of approach becomes more relevant when analyzing data from climate simulations considering scenarios of climate change. The results obtained in terms of high resolution hazard maps and curves may find significant application in different fields, as for example, as the hazard component for multi-risk assessment problems (which is our main interest, see e.g. Marzocchi et al 2012), for planning purposes, or for the design of critical infrastructures with consideration of potential changes occurring in the climate.

We have put forward a Bayesian framework for the analysis and testing of possible non stationarities in extreme events. Our main interest is to produce results with high spatial and temporal resolution; to pursue this requirement we have adopted an individual GBA approach to exploiting as much as possible the capabilities of RCMs to replicate spatial variations in climate, especially in regions with complex orography. Nevertheless, this choice bears intrinsic problems respect to adopting an alternative approach based on spatial pooling of the data (that generally allows a more reliable estimation of high return period events, see e.g., Fowler et al 2005; Hanel et al 2009).

To keep the capacity of GBA reproducing high spatial resolution results and increase the reliability of the results of EV analyses, the approach presented in this paper is composed of four key elements, namely (1) an advanced Bayesian method for the estimation of model parameter values, (2) a rigorous procedure for model

selection, (3) uncertainty assessment and propagation, and (4) the analysis of results taking into account the uncertainties.

Implementing a Bayesian method for the inference of the GEV model parameters under non-stationary conditions has some important advantages since it is a framework that naturally allows incorporating all available sources of information as well as to handle uncertainties. In fact, beyond the information provided by the data, other available sources of information can be easily encoded as a prior density function in the space of the model parameters.

We performed different tests to set the prior state of information; in most of the cases, non-informative or 'poorly' informative priors have had negligible effects on the posterior distribution. However, the use of informative priors resulted very important to preserve the spatial coherence in the results given the 'areal' character of our analyses. The shape parameter ξ, determinant to identify the distribution of the GEV family describing the data and therefore the behavior of the higher extreme intensities, required a special attention because its determination is often subject to numerical instabilities and large uncertainties. For example, it was observed that in some nodes the ξ value exhibits very large uncertainties; in other cases it was found that the value in a given node was inconsistent with the values found in the surrounding nodes. Suspecting that these cases can reflect an anomaly in the solutions, we proposed the use of the more spatially coherent results obtained in the surrounding nodes to create an informative prior for the specific node(s) under suspect. This assumption is motivated by the fact that we can expect the changes in the intensities of extreme events to be associated with variations in the atmospheric conditions at scales larger than the resolution used to generate the data employed in the GBA approach. Furthermore, the input data has not been spatially pooled and the model parameter values are determined independently at each node using different time series; therefore, the parameter values obtained in the nodes around a given node with unstable results can be effectively used to set the prior information for that node with inconsistent results. This approach allowed us to improve the spatial coherence of the results and to reduce uncertainties in some nodes with odd results.

A rigorous method for model selection is a fundamental tool to identify the areas where there is evidence in favor of non-stationary models explaining the data. We have tested different models to describe possible trends in the location parameter of the GEV and found that for both the temperature and precipitation data, a linear trend was the only model performing better than the stationary one in the areas in which evidence against the stationary model exists. This may be due to the relatively short time series used to fit the models. In the simulation considering the RCP4.5 scenario, which between 2010 and 2050 implies an increase of about 3% in the CH_4 and 25% in the CO_2 concentrations, the extreme precipitation is stationary in a wide area of the domain; areas with negative trends are identified at the NE part of the domain around Zanzibar (about -0.3 to -0.6 mm/year), whereas zones with positive trends are clustered at the S (with $\beta_1 \sim 0.6$ to 1.2 mm/year). On the other hand, the temperature extremes are mainly stationary in the inland area, whereas positive trends have been identified at the NE of the domain (correlated with a decreasing trend in precipitation). The slope of the temperature trend in that area is of about 0.02°C/year.

In the simulation considering the RCP8.5 scenario, which implies an increase of about 50% in the CH_4 and about 40% in the CO_2 concentrations in the same time interval, the extreme temperature exhibits non-stationary conditions in the whole domain; a positive trend dominates the inland area with peak values in the range 0.06 to 0.16°C/year, while negative trends are identified at the NE of the domain (as in the other scenario). Interestingly, the results for the precipitation extremes show a similar pattern as that observed with the RCP4.5 scenario; it means that the differences in both scenarios are mainly reflected in the temperature data.

However, to analyse and draw conclusions about the resulting trends in the intensity of extremes (for given exceedance probability values), the uncertainties in these intensity values should also be taken into account. For example, Figs. 7 and 10 (c and d) show that in general, the lower the exceedance probability value, the wider the uncertainty range of the associated intensity. This observation is also evident in the uncertainty bounds obtained in the temperature and precipitation trends (as shown, respectively, in Figs. 8c and 12c). These examples indicate that even when there is evidence in favor of a non-stationary model, the resulting change in intensity after a given time window (e.g. after 30 years) might not be completely meaningful when the obtained intensities have large uncertainties (with respect to the order of magnitude of the change); this issue is evident for example in the trend in precipitation with 1% exceedance probability shown in Fig. 12c.

The numerical problems when performing inference on ξ are not the only element of interest about this parameter. Its value, in fact, determines the shape of the distribution tails and therefore it is fundamental for the hazard assessment (e.g., to understand the behaviour

of the more extreme events). For example, $\xi < 0$ indicates an upper-side bounded distribution (Weibull) which physically may represent processes allowing the definition of a kind of 'maximum event'. Conversely, $\xi > 0$ (Frechét type) indicates a distribution bounded on the lower-side (and therefore a process with a minimum intensity value) and with a heavy upper tail. Finally, the Gumbel is unbounded and defined on the real axis (long tails). Considering the results of the EV analyses, marked differences in the ξ parameter have been found for the temperature and the precipitation data. In both cases, the higher values of ξ are distributed in the N and NE part of the domain. However, for the temperature data, the dominating values of the shape parameter are $\xi < 0$, indicating that the upper-side bounded Weibull is the dominating distribution of the GEV family for these data. Conversely, for the precipitation data $\xi > 0$ in the whole domain, indicating that the GEV models are of Frechét type (i.e. unbounded upper tail).

In the case of precipitation only, we have generated ensembles of precipitation fields with higher spatial resolution than that provided by the RCM by applying a further stochastic downscaling approach. The advantage of using stochastic downscaling consists in the possibility to generate an ensemble of stochastic realizations of small-scale precipitation fields providing a measure of the uncertainty associated to the extreme precipitation intensity estimates. Interestingly, in the specific case analyzed here, the statistics of precipitation extremes at small scales (1 km) produced after the downscaling procedure is similar to that obtained at the original regional model resolution (8 km); it indicates that for impact studies, the spatial resolution of the RCM outputs in this area is sufficiently high to represent the distribution of extreme daily precipitation. We hypothesize that the absence of additional extremes in the downscaled COSMO-CLM precipitation can be attributed to quite long temporal accumulation period of the modeled data (1 day), compared with the high spatial resolution achieved by downscaling.

There is a number of directions in which we expect to move forward with this work. The lack of data from an observation network to validate the results obtained using the synthetic data generated by the RCM simulations is a limitation of our study. Therefore, applying the presented methodology to an area where both observed and simulated data is available will allow us also to validate the results of the analysis of extremes obtained from the simulated data. An important issue to be considered is to assess the possibility to run an ensemble of different RCM runs in order to consider the modeling uncertainties as well. Finally, a further development to improve the performance of the method by reducing the large uncertainties associated with the lower probability extremes could be done, and a possible approach to explore is to develop a spatial pooling strategy in coherent agreement with the outlined strategy to define informative priors.

Acknowledgements The manuscript was greatly improved by timely and constructive comments from two anonymous reviewers. This research has been developed in the framework of the FP7 European project CLUVA (Climate change and Urban Vulnerability in Africa), grant No. 265137.

A The GEV family of distributions (Appendix A)

Denoting daily observations by $x_1, x_2, \ldots$, the classical model for extremes is obtained by analyzing the behavior of $\mathbf{z}_i = \max\{x_1, x_2, \ldots, x_i\}$ for large values of i. Asymptotic considerations suggest that the distribution of a series of measures of extreme physical events extracted from long sequences of data approaches one of the three families of distributions that are combined into the GEV (e.g., Jenkinson 1955; Martins and Stedinger 2000; Coles 2001). The GEV family of distributions has a distribution function of the form:

$$G(z|\mu,\sigma,\xi) = \exp\left\{-\left[1+\xi\left(\frac{z-\mu}{\sigma}\right)\right]^{-1/\xi}\right\} \tag{8}$$

defined on the set $\{z : 1+\xi(z-\mu)/\sigma > 0\}$, and with parameter space $(\mu,\sigma,\xi) : \mu \in \mathbb{R}$ (location parameter), $\sigma \geq 0$ (scale parameter), and $\xi \in \mathbb{R}$ (shape parameter) (e.g. Coles 2001). The Frechét (or Type II) and Weibull (or type III) classes of EV distribution correspond respectively to the cases $\xi > 0$ and $\xi < 0$ in this parameterization. These two cases have bounds in the domain of z: for instance, $\mu - \sigma/\xi \leq z < \infty$ for $\xi > 0$, and $-\infty < z \leq \mu - \sigma/\xi$ for $\xi < 0$. The special case of the GEV distribution obtained for $\xi \to 0$ is the Gumbel (or Type I) class, with distribution function:

$$G(z|\mu,\sigma,\xi) = \exp\left\{-\exp\left[-\left(\frac{z-\mu}{\sigma}\right)\right]\right\}; z \in \mathbb{R} \tag{9}$$

B Bayesian inference of model parameters (Appendix B)

In Bayesian data analysis the model parameters are treated as random variables to account for the imperfect knowledge of their exact values. Beyond the information provided by the data, a Bayesian framework allows to incorporate other sources of information that may be available and that may be encoded to construct the prior density function of the model parameters. The prior information may be available from different sources as past studies in the same or similar regions, global or regional information, or subjective information of experts. The important point to be outlined is that the prior distribution must be formulated independently of the data used for the likelihood. The prior is then a probability distribution which should reflect the knowledge (or lack of) about a parameter before seeing the data. The Bayes theorem is then used to update the prior probability density with the

information provided by the data to obtain the posterior distribution:

$$p(\theta|\mathbf{z}) = \frac{f(\mathbf{z}|\theta)\pi(\theta)}{\int f(\mathbf{z}|\theta)\pi(\theta)\mathrm{d}\theta} \quad (10)$$

where $\mathbf{z} = (z_1, z_2, \ldots, z_n)$ is the vector of data, $\pi(\theta)$ the prior density of the model parameters, $f(\mathbf{z}|\theta)$ the likelihood of the data, and $p(\theta|\mathbf{z})$ the posterior probability density, which is the conditional distribution of the parameters given the observed data. All inference about the parameters is based on the posterior distribution.

In most multi-dimensional cases, posterior simulations are needed for Bayesian inference. To get samples from the posterior distribution we use a Markov chain Monte Carlo (MCMC) method. The MCMC is a general method based on drawing values of θ from approximate distributions and then correcting those draws to better approximate the target posterior distribution, $p(\theta|\mathbf{z})$. The samples are drawn sequentially with the distribution of the sampled draws depending on the last value drawn (hence, the draws form a Markov Chain). The key to MCMC simulations is to create a Markov process whose stationary distribution is the specified $p(\theta|\mathbf{z})$ and run the simulations long enough that the distribution of the current draws is close enough to this stationary distribution (e.g., Gelman et al 2004). In our application, we construct the Markov chains via the Metropolis-Hastings algorithm (Metropolis and Ulam 1949; Metropolis et al 1953). After running the Markov chain, we remove the burn-in period and check the convergence of the simulated sequences. Different approaches are available for this procedure (e.g., Geweke 1992; Geyer 1992; Gelman and Rubin 1992); in our analyses we have implemented the method proposed by Geweke (1992) (often referred as the Geweke-z-score).

C Bayes Factor: The Laplace-Metropolis estimator (Appendix C)

The Bayes factor, B_{kl}, for comparing model M_k to Model M_l for observed data $\mathbf{z}$, is the ratio of the posterior odds for M_k against M_l to the prior odds. When the models M_k and M_l are equally probable a priori, then B_{kl} reduces to:

$$B_{kl} = \frac{f(\mathbf{z}|M_l)}{f(\mathbf{z}|M_k)} \quad (11)$$

It implies computing the integrated likelihoods for model M_m (also called the marginal likelihood, marginal probability of the data, or predictive probability of the data) that has the form

$$f(\mathbf{z}|M_m) = \int f(\mathbf{z}|\theta_m, M_m) f(\theta_m|M_m) d\theta_m \quad (12)$$

where θ_m is the vector of parameters in model M_m, and $f(\theta_m|M_m)$ is its prior density (for more details see e.g., Kass and Raftery 1995; Lewis and Raftery 1997b).

To estimate the marginal likelihoods for the Bayes factor calculation we have implemented the Laplace-Metropolis estimator (Raftery 1996; Lewis and Raftery 1997a), which uses the posterior simulation output to estimate the integrated likelihoods. Letting $h(\theta) \equiv \log\{f(\theta)f(\mathbf{z}|\theta)\}$ (the notation showing the conditioning respect to M_m –as in Eq. 12– has been dropped for simplicity) and applying the Laplace approximation for an integral, the following approximation for the integrated likelihood is obtained (Raftery 1996; Lewis and Raftery 1997a):

$$f(\mathbf{z}) \approx (2\pi)^{P/2} |\mathbf{H}^*|^{1/2} f(\theta^*) f(\mathbf{z}|\theta^*) \quad (13)$$

where θ^* is the value of θ at which h attains its maximum and $\mathbf{H}^*$ is minus the inverse Hessian of h evaluated at θ^* (Lewis and Raftery 1997a). For numerical reasons we use Eq. 13 in a logarithmic scale ($\log\{f(\mathbf{z})\}$). To calculate the Laplace-Metropolis estimator we use the posterior samples generated by the Metropolis-Hastings algorithm to estimate both θ^* and $\mathbf{H}^*$. In practice, the components of θ^* are estimated calculating the component-wise posterior medians from the sample, whereas $\mathbf{H}^*$, being asymptotically equal to the posterior variance matrix, is estimated using the sample covariance matrix of the posterior simulation output.

References

Atyeo J, Walshaw D (2012) A region-based hierarchical model for extreme rainfall over the UK, incorporating spatial dependence and temporal trend. Environmetrics 23(6):509–521, DOI 10.1002/env.2155, URL http://dx.doi.org/10.1002/env.2155

Beaulieu C, Seidou O, Ouarda T, Zhang X, Boulet G, Yagouti A (2008) Intercomparison of homogenization techniques for precipitation data. Water Resources Research 44(2):W02,425

Bell TL (1987) A space-time stochastic model of rainfall for satellite remote sensing studies. J Geophys Res 92:9631–9643

Bellprat O, Kotlarski S, Lüthi D, Schär C (2012) Objective calibration of regional climate models. Journal of Geophysical Research: Atmospheres 117(D23), DOI 10.1029/2012JD018262, URL http://dx.doi.org/10.1029/2012JD018262

Bohm U, Kuchen M, Ahrens W, Block A, Hauffe D, Keuler B, Rockel B, Will A (2006) CLM - The Climate Version of LM: Brief Description and Long-Term Applications. COSMO Newsletter 6:225–235

Brussolo E, von Hardenberg J, Ferraris L, Rebora N, Provenzale A (2008) Verification of Quantitative Precipitation Forecasts via Stochastic Downscaling. J Hydrometeor 9:1084–1094

Bucchignani E, Sanna A, Gualdi S, Castellari S, Schiano P (2013) Simulation of the climate of the XX century in the Alpine space. Natural Hazards 67:981–990, DOI 10.1007/s11069-011-9883-82010

Cannon A (2010) A flexible nonlinear modelling framework for nonstationary generalized extreme value analysis in hydroclimatology. Hydrological Processes 24(6):673–685

Carter TR, Jones JN, Lu X, Bhadwal S, Conde C, Mearns LO, O'Neill BC, Rounsevell MDA, Zurek MB (2007) New assessment methods and the characterisation of future conditions. In: Parry ML, Canziani OF, Palutikof JP, Linde PJVD, Hanson CE (eds) Climate Change 2007. Impacts, Adaptation and Vulnerability. Contribution of Working Group II to the Fourth Assessment Report of the Intergovernmental Panel on Climate Change, Cambridge University Press., Cambridge, UK, pp 133–171

Coles S (2001) An introduction to statistical modeling of extreme values. Springer series in statistics, Springer-Verlag London limited

Davison AC, Padoan SA, Ribatet M (2012) statistical modelling of spatial extremes. Statist Sci 27(2):161–186, DOI 10.1214/11-STS376

D'Onofrio D, Palazzi E, von Hardenberg J, Provenzale A, Calmanti S (2014) Stochastic rainfall downscaling of climate models. Journal of Hydrometeorology 15:830–843, DOI 10.1175/JHM-D-13-096.1

Ekström M, Fowler H, Kilsby C, Jones P (2005) New estimates of future changes in extreme rainfall across the {UK} using regional climate model integrations. 2. Future estimates and use in impact studies. Journal of Hydrology 300(1–4):234–251, DOI 10.1016/j.jhydrol.2004.06.019, URL http://www.sciencedirect.com/science/article/pii/S0022169404002822

El-Adlouni S, Favre AC, Bobee B (2006) Comparison of methodologies to assess the convergence of Markov Chain Monte Carlo methods. Computational Statistics and Data Analysis 50(10):2685–2701

El Adlouni S, Ouarda T, Zhang X, Roy R, Bobée B (2007) Generalized maximum likelihood estimators for the nonstationary generalized extreme value model. Water Resources Research 43(3):W03,410

Fowler H, Ekström M, Kilsby C, Jones P (2005) New estimates of future changes in extreme rainfall across the {UK} using regional climate model integrations. 1. Assessment of control climate. Journal of Hydrology 300(1–4):212–233, DOI 10.1016/j.jhydrol.2004.06.017, URL http://www.sciencedirect.com/science/article/pii/S0022169404003111

Gelman A, Rubin D (1992) Inference from Iterative Simulation Using Multiple Sequences. Statist Sci 7(4):457–472, DOI 10.1214/ss, URL http://projecteuclid.org/euclid.ss/1177011136

Gelman A, Carlin J, Stern H, Rubin D (2004) Bayesian Data Analysis, II edn. Chapman and Hall/CRC.

Geweke J (1992) Evaluating the accuracy of sampling-based approaches to the calculation of posterior moments, In: Bayesian Statistics 4, J.M. Bernardo, J.O. Berger, A.P. Dawid, and A.F. Smith (eds.), Oxford University Press, pp 169–193

Geyer CJ (1992) Practical Markov Chain Monte Carlo. Statist Sci 7(4):473–483, DOI 10.1214/ss, URL http://projecteuclid.org/euclid.ss/1177011137

Giorgi F, Hurrell JW, Mariucci MR (1997) Elevation dependency of the surface climate change signal: a model study. J Climate 10:288–296, DOI 10.1175/1520-0442(1997)010

Gualdi S, Somot S, Li L, Artale V, Adani M, Belluci A, Braun A, Calmanti S, Carillo A, Dell'Aquila A, Deque M, Dubois C, Elizalde A, Harzallah A, Jacob D, L'Heveder B, May W, Oddo P, Ruti P, Sanna A, Sannino G, Scoccimarro E, Sevault F, Navarra A (2013) The CIRCE Simulations: Regional Climate Change Projections with Realistic Representation of the Mediterranean Sea. Bull Amer Meteor Soc 94:65–81, DOI 10.1175/BAMS-D-11-00136.1

Hanel M, Buishand TA, Ferro CAT (2009) A nonstationary index flood model for precipitation extremes in transient regional climate model simulations. Journal of Geophysical Research: Atmospheres 114(D15), DOI 10.1029/2009JD011712, URL http://dx.doi.org/10.1029/2009JD011712

von Hardenberg J, Ferraris L, Rebora N, Provenzale A (2007) Meteorological uncertainty and rainfall downscaling. Nonlinear Proc Geophys 14:193–199

Houghton J, Ding Y, Griggs DJ, Noguer M, van der Linden PJ, Dai X, Maskell K, Johnson CA (eds) (2001) Climate Change 2001: The Scientific Basis. Cambridge Uni- versity Press

Hrafnkelsson B, Morris JS, Baladandayuthapani V (2012) Spatial modeling of annual minimum and maximum temperatures in Iceland. Meteorology and Atmospheric Physics 116(1-2):43–61, DOI 10.1007/s00703-010-0101-0

Huth R, Kysely J, Pokorna L (2000) A GCM Simulation of Heat Waves, Dry Spells, and Their Relationships to Circulation. Climatic Change 46(1-2):29–60, DOI 10.1023/A:1005633925903

IPCC (2012) Managing the Risks of Extreme Events and Disasters to Advance Climate Change Adaptation. Cambridge University Press, Cambridge, UK, and New York, NY, USA

IPCC (2013) Climate Change 2013: The Physical Science Basis. Contribution of Working Group I to the Fifth Assessment Report of the Intergovernmental Panel on Climate Change. Cambridge University Press, Cambridge, UK, and New York, NY, USA

Jain S, Lall U (2001) Floods in a changing climate: Does the past represent the future? Water Resources Research 37(12):3193–3205

Jeffreys H (1961) Theory of Probability, 3rd edn. Oxford University Press, Oxford, U. K.

Jenkinson AF (1955) The frequency distribution of the annual maximum (or minimum) values of meteorological elements. Quarterly Journal of the Royal Meteorological Society 81:158–171

Kass RE, Raftery AE (1995) Bayes Factors. Journal of the American Statistical Association 90(430):773–795

Katz R (2010) Statistics of extremes in climate change. Climatic Change 100(1):71–76

Katz R, Parlange M, Naveau P (2002) Statistics of extremes in hydrology. Advances in water resources 25(8-12):1287–1304

Khaliq M, Ouarda T, Ondo JC, Gachon P, Bobée B (2006) Frequency analysis of a sequence of dependent and/or non-stationary hydro-meteorological observations: A review. Journal of Hydrology 329(3–4):534–552, DOI 10.1016/j.jhydrol.2006.03.004, URL http://www.sciencedirect.com/science/article/pii/S0022169406001302

Koutsoyiannis D (2004) Statistics of extremes and estimation of extreme rainfall: II. Empirical investigation of long rainfall records / Statistiques de valeurs extrêmes et estimation de précipitations extrêmes: II. Recherche empirique sur de longues séries de précipitations. Hydrological Sciences Journal 49(4):591–610, DOI 10.1623/hysj.49.4.591.54424, http://www.tandfonline.com/doi/pdf/10.1623/hysj.49.4.591.54424

Kysely J (2002) Probability estimates of extreme temperature events: stochastic modelling approach vs. extreme value distributions. Stud Geophys Geod 46:93–112

Kysely J (2010) Recent severe heat waves in central Europe: how to view them in a long-term prospect? International Journal of Climatology 30(1):89–109, DOI 10.1002/joc.1874

Lewis S, Raftery A (1997a) Estimating Bayes factors via posterior simulation with the Laplace-Metropolis estimator. Journal of the American Statistical Association 92(438):648–655, DOI 10.1080/01621459.1997.10474016

Lewis SM, Raftery AE (1997b) Estimating Bayes Factors via Posterior Simulation with the Laplace-Metropolis Estimator. Journal of the American Statistical Association 92(438):648–655

Lovejoy S, Mandelbrot B (1985) Fractal properties of rain and a fractal model. Tellus 37A:209–232

Martins E, Stedinger J (2000) Generalized maximum-likelihood generalized extreme-value quantile estimators for hydrologic data. Water Resources Research 36(3):737–744

Marzocchi W, Garcia-Aristizabal A, Gasparini P, Mastellone ML, Di Ruocco A (2012) Basic principles of multirisk assessment: a case study in Italy. Natural Hazards 62(2):551–573

Menabde M, Seed A, Harris D, Austin G (1997) Selfsimilar random fields and rainfall simulations. J Geophys Res C Oceans 102D:13,509–13,515

Metropolis N, Ulam S (1949) The Monte Carlo method. J Amer Stat Assoc 44:335–341

Metropolis N, Rosenbluth A, Rosenbluth M, Teller A, Teller E (1953) Equation of state calculations by fast computing machines. J Chem Phys 21:1081–1092

Moss RH, Edmonds JA, Hibbard KA, Manning MR, Rose SK, van Vuuren DP, Carter TR, Emori S, Kainuma M, Kram T, Meehl GA, Mitchell JFB, Nakicenovic N, Riahi K, Smith SJ, Stouffer RJ, Thomson AM, Weyant JP, Wilbanks TJ (2010) The next generation of scenarios for climate change research and assessment. Nature 463(7282):747–756, DOI 10.1038/nature08823, URL http://www.nature.com/nature/journal/v463/n7282/suppinfo/nature08823_S1.html, 10.1038/nature08823

Newton MA, Raftery AE (1994) Approximate Bayesian Inference with the Weighted Likelihood Bootstrap. Journal of the Royal Statistical Society Series B 56(1):3–48

Ouarda T, El-Adlouni S (2011) Bayesian Nonstationary Frequency Analysis of Hydrological Variables. JAWRA Journal of the American Water Resources Association 47(3):496–505

Perica S, Foufoula-Georgiou E (1996) Model for multiscale disaggregation of spatial rainfall based on coupling meteorological and scaling description. J Geophys Res 101(D21):26,347–26,361

Raftery A (1995) Bayesian Model Selection in Social Research. Social Methodology 25:111–163

Raftery AE (1996) Hypothesis testing and model selection. In: Gilks WR, Richardson S, Spiegelhalter DJ (eds) Markov Chain Monte Carlo in practice, Chapman and hill, pp 165–187

Raftery AE, Newton MA, Satagopan JM, Krivitsky PN (2007) Estimating the Integrated Likelihood via Posterior Simulation Using the Harmonic Mean Identity. Bayesian Statistics 8:1–45

Rebora N, Ferraris L, von Hardenberg J, Provenzale A (2006a) Rainfall downscaling and flood forecasting: a case study in the Mediterranean area. Nat Hazards Earth Syst Sci 6:611–619

Rebora N, Ferraris L, von Hardenberg J, Provenzale A (2006b) RainFARM: Rainfall Downscaling by a Filtered AutoRegressive Model. J Hydrometeor 7:724–738

Rockel B, Will A, Hense A (2008) The Regional Climate Model COSMO-CLM (CCLM). Meteorologische Zeitschrift 17:347–348

Sang H, Gelfand A (2010) Continuous Spatial Process Models for Spatial Extreme Values. Journal of Agricultural, Biological, and Environmental Statistics 15:49–65, DOI 10.1007/s13253-009-0010-1, URL http://dx.doi.org/10.1007/s13253-009-0010-1

Scotto MG, Barbosa SM, Alonso AM (2011) Extreme value and cluster analysis of European daily temperature series. Journal of Applied Statistics 38(12):2793–2804, DOI 10.1080/02664763.2011.570317, URL http://www.tandfonline.com/doi/abs/10.1080/02664763.2011.570317, http://www.tandfonline.com/doi/pdf/10.1080/02664763.2011.570317

Seidou O, Ramsay A, Nistor I (2011) Climate change impacts on extreme floods II: improving flood future peaks simulation using non-stationary frequency analysis. Natural Hazards pp 1–12

Seidou O, Ramsay A, Nistor I (2012) Climate change impacts on extreme floods I: combining imperfect deterministic simulations and non-stationary frequency analysis. Natural Hazards pp 1–13, DOI 10.1007/s11069-011-0052-x

Siliverstovs B, Ötsch R, Kemfert C, Jaeger CC, Haas A, Kremers H (2010) Climate change and modelling of extreme temperatures in Switzerland. Stochastic Environmental Research and Risk Assessment 24(2):311–326, DOI 10.1007/s00477-009-0321-3

Solomon S, Qin D, Manning M, Chen Z, Marquis M, Averyt KB, Tignor M, Miller HL (eds) (2007) Climate Change 2007: The Physical Science Basis. Cambridge Univer- sity Press

Sorooshian S, Hsu Kl, Coppola E, Tomassetti B, Verdecchia M, (Eds) GV (2008) Hydrological Modelling and the Water Cycle Coupling the Atmospheric and Hydrological Models, Water Science and Technology Library, vol 63

Stephenson DB, Diaz HF, Murnane RJ (2008) Definition, diagnosis, and origin of extreme weather and climate events, Cambridge University Press, Cambridge, UK, pp 11–23. in: Climate Extremes and Society

Steppeler J, Doms G, Schattler U, Bitzer H, Gassmann A, Damrath U, Gregoric G (2003) Meso-gamma scale forecasts using the nonhydrostatic model LM. METEOROLOGY AND ATMOSPHERIC PHYSICS 82(1-4):75–96, DOI 10.1007/s00703-001-0592-9, 4th SRNWP Workshop on Nonhydrostatic Modelling, BAD ORB, GERMANY, SEP, 2001

Waymire EC, Gupta VK, Rodriguez-Iturbe I (1984) A spectral theory of rainfall intensity at the meso-beta scale. Water Resour Res 20:1453–1465

Zhang X, Zwiers F, Li G (2004) Monte Carlo experiments on the detection of trends in extreme values. Journal of Climate 17(10):1945–1952

Zwiers F, Kharin VV (1998) Changes in the extremes of the climate simulated byCCCGCM2 under CO2 doubling. Journal of Climate 11:2200–2222